J. Fluid Mech. (1986), *vol.* 172, *pp.* 419–451
Printed in Great Britain

Analysis of chaotic mixing in two model systems

By D. V. KHAKHAR,
Department of Chemical Engineering, Goessmann Laboratory,
University of Massachusetts, Amherst, MA 01003, USA

H. RISING
Department of Mathematics, University of Massachusetts, Amherst, MA 01003, USA

AND J. M. OTTINO
Department of Chemical Engineering, Goessmann Laboratory,
University of Massachusetts, Amherst, MA 01003, USA

(Received 24 September 1985 and in revised form 1 April 1986)

We study the chaotic mixing in two periodic model flows, the 'tendril–whorl' flow and the 'Aref-blinking-vortex' flow, with the objective of supplying evidence for the primary mechanisms responsible for mixing in two-dimensional deterministic flows. The analysis is based on tools of dynamical systems theory but it is clear that the mixing problem generates several questions of its own: low periodic points and horseshoes dominate the picture, since we want to achieve mixing quickly; Poincaré sections, popular in dynamical systems analyses, might give misleading information with regard to dispersion at short times. Our analysis shows that both flows are able to stretch and fold material lines well below the lengthscale of the flows themselves. The inner workings of the two systems are revealed by studying the local and global bifurcations. Computations for the blinking-vortex system indicate the existence of an optimum period at which the average efficiency is maximized, whereas the intensity of segregation – a classical parameter in mixing studies – decays rapidly to an asymptotic value in the globally chaotic region. Even though our flows are not turbulent the results might have some implications for pointing to the limits of similar studies in actual turbulent flows (e.g. line stretching).

1. Introduction

It seems to be impossible to develop a comprehensive theory of the mixing of fluids; complications stem from both *fluids* and *flows*. The *fluids* may be rheologically complex, miscible, immiscible or partially miscible, reacting or not, so that obtaining the velocity field in many situations of practical interest seems to be impossible. As we shall see, even if the velocity field is known, the *flow* or motion of the fluid particles may easily be complex enough to resist detailed theoretical and computational analyses.

Usually, the starting point of a mixing process is a mixture segregated on a large scale consisting of striations or large blobs. Mechanical mixing causes the striations and blobs to stretch by several orders of magnitude, which in the case of immiscible fluids break into smaller blobs and droplets, the stretching and breakup related in a complicated way to the velocity field. In the case of miscible fluids, of course, molecular diffusion becomes the controlling process once striations are reduced to small enough lengthscales. An analytical description of the velocity field in most such

systems is impossible, and in many cases even a computational analysis is beyond the scope of modern computers. The theoretical construction must start from the simple and evolve towards the complex.

On defining mixing with *passive* and *active* interfaces (Aref & Tryggvason 1984), however, the following conceptual simplification is possible. In the case of mixing with *passive* interfaces the motion is topological and the interfaces are simply material surfaces which do not affect the flow. *Active* interfaces, on the other hand, interact with the flow and modify it, as in the case of interfaces between immiscible fluids. It is then obvious that in constructing a general theoretical framework for mixing a minimum requirement is to describe mixing in terms of the stretching of passive interfaces and then to add, possibly at small scales, the effect of active interfaces, diffusion, reaction, etc. (Ottino 1982).

Clearly, if the velocity field is given our problem is one of kinematics. However, one of the biggest misconceptions in mixing is that once the velocity field is obtained, the problem is essentially solved. As we shall see, the essence of mixing lies in the *flow* or the 'motion' of the fluid particles (Ottino 1982), which in the case of nonlinear velocity fields can be extremely complicated. Very simple looking velocity fields can produce quite extraordinary behaviour. For simplicity, we consider here the case of two-dimensional area-preserving flows that are periodic in time. An additional, and important, reason is that there is a considerable amount of theoretical guidance for this case.

A study of the basic building blocks of a flow that are responsible for chaotic advection occupies an important position in a theory of mixing; however, at the moment we cannot anticipate what flows will be capable of displaying such behaviour. The objective of this work is to provide evidence of the primary mechanisms responsible for mixing in two-dimensional deterministic flows. We first briefly define some of the terms we use (the reader is referred to appropriate sources for details), and then present the analysis of two complementary model flows, the 'tendril–whorl' flow, and the 'Aref-blinking-vortex' flow. The tendril–whorl flow is a periodic sequence of strong and weak flows, and in some sense is a simplified local description of a complex flow. The motion of particles in this case is unbounded, and most of the mixing occurs in a region around the origin with particles entering and leaving the mixing zone through 'conduits' so that it may be regarded as a 'continuous' mixing system. The blinking-vortex flow on the other hand is composed of a sequence of weak flows and has bounded particle trajectories. The mixing zone in this case is well defined and closed hence it may be regarded as a 'batch' mixing system.

2. Mathematical background

The equations describing the trajectory of a fluid particle for a given velocity field $\boldsymbol{v}$ are

$$\dot{\boldsymbol{x}} = \boldsymbol{v}(\boldsymbol{x}, t), \tag{1}$$

where, in general, the velocity field may be time dependent. A solution to the above equation exists at least locally, and is given by

$$\boldsymbol{x} = \boldsymbol{f}_t(\boldsymbol{x}_0), \tag{2a}$$

where $\boldsymbol{x}$ denotes the position at time t of a particle initially at $\boldsymbol{x}_0$. In continuum mechanics (Truesdell & Toupin 1960) (2a) is called the 'motion'. In the context of our future discussion we refer to it as the *flow*. When flows are periodic in time, as

is the case with the model systems we analyse below, the motion may be expressed as a mapping

$$\boldsymbol{x} = \boldsymbol{f}_T^n(\boldsymbol{x}_0) = \boldsymbol{f}^n(\boldsymbol{x}_0), \tag{2b}$$

where n is the number of cycles of flow, and T is the time period. In this case, the trajectory of the particle is represented by a sequence of points rather than a continuous curve.

That a system such as (1) is capable of chaotic behaviour was demonstrated by Hénon (1966) who studied the problem on a suggestion of V. I. Arnold, and for the case of two-dimensional flows by Aref (1984), who recognized that (1), restricted to isochoric flows, is a Hamiltonian system with one or two degrees of freedom. The qualitative theory of differential equations indicates that 'chaotic' behaviour in dynamical systems is the rule rather than the exception. Comprehensive treatment of the fundamentals of 'chaotic' dynamical systems may be found in the recent books by Lichtenberg & Lieberman (1982), and Guckenheimer & Holmes (1983), and in the excellent review article by Helleman (1980). The book by Lichtenberg & Lieberman primarily addresses Hamiltonian systems, and is especially useful.

The key to the understanding of the complex behaviour of chaotic flows resides in the structure of periodic points, and the local and global bifurcations of the flow. A single transverse intersection between the *stable* and *unstable manifolds* of a *hyperbolic periodic point* is sufficient to produce chaotic behaviour, and can be explained in terms of the wild behaviour of the manifolds that results (Lichtenberg & Lieberman 1982, p. 170). A *periodic point* of period p of a mapping

$$\boldsymbol{f}\colon \boldsymbol{x} \to \boldsymbol{f}(\boldsymbol{x})$$

is defined as

$$\boldsymbol{x}^* = \boldsymbol{f}^p(\boldsymbol{x}^*),$$

and the periodic point is *hyperbolic* if the Jacobian of the mapping iterated p times evaluated at the periodic point, $\mathrm{D}\boldsymbol{f}^p(\boldsymbol{x}^*)$, has no eigenvalues of unit modulus, where

$$\mathrm{D}\boldsymbol{f}^p(\boldsymbol{x}) = \left(\frac{\partial f_i^p}{\partial x_j}\right).$$

The *stable* and *unstable manifolds* of a period-p hyperbolic periodic point are invariant sets defined as

$$\omega_p^{\mathrm{S}}(\boldsymbol{x}^*) = \{\boldsymbol{x} \,|\, \boldsymbol{f}^{np}(\boldsymbol{x}) \to \boldsymbol{x}^* \quad \text{as } n \to \infty\},$$

$$\omega_p^{\mathrm{U}}(\boldsymbol{x}^*) = \{\boldsymbol{x} \,|\, \boldsymbol{f}^{np}(\boldsymbol{x}) \to \boldsymbol{x}^* \quad \text{as } n \to -\infty\},$$

so that if a point belongs to a manifold all its forward and reverse images iterated p times also belong to the manifold. A transverse intersection between the stable and unstable manifold of a periodic point is referred to as a transverse *homoclinic* point. Transverse intersections between the manifolds of different periodic points are known as transverse *heteroclinic* points, and we refer to the wild behaviour of the manifolds that results as heteroclinic or homoclinic behaviour. In the case of regular flows, the manifolds join smoothly and none of the above behaviour occurs.

The main impediments for mixing in two-dimensional flows are 'KAM curves' which are invariant curves formed by quasi-periodic regular trajectories and act as barriers to transport. The existence of such curves in the neighbourhood of an *elliptic* periodic point was established by the Kolmogorov–Arnold–Moser (KAM) Theorem (Guckenheimer & Holmes 1983, p. 219), their survival being related to the irrationality

of the rotation number (Guckenheimer & Holmes 1983, p. 295; Lichtenberg & Lieberman 1982, p. 159), which depends on the frequency of rotation of the trajectory around the periodic point. A periodic point is said to be *elliptic* if the eigenvalues of the Jacobian evaluated at the periodic point are complex and of magnitude 1. Typically such curves abound in the neighbourhood of an elliptic periodic point when the nonlinear perturbation in the neighbourhood of the periodic point is small enough, forming an *island* of fluid which does not mix with the rest of the fluid, the size of which depends on the outermost surviving KAM curve.

In the following analysis, we study the local flow in the neighbourhood of periodic points and then consider the global flow in terms of interactions of the manifolds of the periodic points. For the blinking-vortex system we also calculate the Liapunov exponent, the average efficiency, and the intensity of segregation, all of which are useful in the quantitative evaluation of a mixing process.

3. The tendril–whorl mapping

The tendril–whorl flow (Rising 1986) is a simple periodic flow, each period being composed of a homogeneous extensional flow followed by a nonlinear rotational flow. It provides an insight into the local behaviour of more complex flows which, from a Lagrangian point of view, may be decomposed into an extensional and rotational component both varying with time. The simplicity of the system allows a reasonably detailed analysis of which we can illustrate the variety of behaviour that is possible, and somehow expected of more complex flows.

The velocity field over a single period of the flow described above is given by

$$\left.\begin{aligned} v_x &= -\epsilon x, \\ v_y &= \epsilon y, \end{aligned}\right\} \quad 0 < t < T_{\text{ext}},$$

$$\left.\begin{aligned} v_r &= 0, \\ v_\theta &= -\omega(r), \end{aligned}\right\} \quad T_{\text{ext}} < t < T_{\text{ext}} + T_{\text{rot}},$$

where T_{ext} is the duration of time for which the extensional flow exists and T_{rot} the time for which the rotational flow exists. The function $\omega(r)$ is a positive quantity and specifies the rate of rotation, which varies only in the radial direction. The above velocity field can easily be integrated over a single period to give the mappings

$$f_{\text{ext}}\colon (x, y) \to (x/\alpha, \alpha y), \quad f_{\text{rot}}\colon (r, \theta) \to (r, \theta + \Delta\theta),$$

which describe the motion of a fluid particle over a single period $(T_{\text{ext}} + T_{\text{rot}})$. In the above equations we have put $\alpha = \exp(\epsilon T_{\text{ext}})$ and $\Delta\theta = -\omega(r)\, T_{\text{rot}}/r$. When $\omega(r)$ is chosen appropriately, the mappings composed together deform material lines into 'tendrils' and 'whorls' (see Berry *et al.* 1979) thus we refer to the mapping as the tendril–whorl (TW) mapping. In what follows we take the rotation to be of the form

$$\Delta\theta = -Br\, \mathrm{e}^{-r},$$

where B is a constant proportional to T_{rot}. The flow defined above is unbounded, and far from the origin is essentially an extensional flow, the rotational flow decaying exponentially with r.

4. Local bifurcations of the tendril–whorl mapping

The period-1 periodic points of the TW mapping are given in polar coordinates by

$$\theta^* = \tan^{-1}(1/\alpha),$$
$$Br^* \exp(-r^*) = \tan^{-1}\{\tfrac{1}{2}(\alpha - 1/\alpha)\} + 2\pi n \quad (n = 0, 1, \ldots, M),$$

where

$$M = \text{Integer}\left(\frac{-\Delta\theta(r^*) + \tan^{-1}(\alpha)}{2\pi}\right).$$

When $M = 0$, the equations reduce to

$$\theta^* = \tan^{-1}(1/\alpha), \quad r^* \exp(1 - r^*) = 1/\beta,$$

where

$$\beta = \frac{Be}{\tan^{-1}\{(\alpha - 1/\alpha)/2\}}.$$

In this form we notice that the angular position of the periodic points depends only on α, and the radial position on β. It is easy to see that the origin is a periodic point of the flow for all parameter values; in addition there may be two or four or more period-1 periodic points depending on the value of β, as we show below.

The function $r\,e^{(1-r)}$ is non-negative for all r and has a single maximum at $r = 1$ with a maximum value of 1. Thus for $\beta < 1$ the equation for the radial position has no solution and there are no period-1 periodic points other than the origin. At $\beta = 1$ two additional periodic points are born at $r^* = 1$, and $\theta^* = \tan^{-1}(1/\alpha)$ and $\theta^* = \tan^{-1}(1/\alpha) + \pi$. For $\beta > 1$ each of the above periodic points splits into two, one at $r^* > 1$ and one at $r^* < 1$, both pairs maintaining their respective angular positions. The above scenario repeats itself each time

$$\beta = 1 + \frac{2\pi M}{\tan^{-1}\{\frac{1}{2}(\alpha - 1/\alpha)\}}.$$

In what follows, we consider $\beta < 1 + 4\pi$ so that $M = 0$.

The characteristic equation for the eigenvalues of a two-dimensional mapping is given by

$$\lambda^2 - \text{tr}(\mathrm{D}f)\,\lambda + \det(\mathrm{D}f) = 0,$$

where $\mathrm{D}f$ is the Jacobian of the mapping. In the case of area-preserving mappings $\det(\mathrm{D}f) = 1$ so that we obtain

$$\lambda_{1,2} = \tfrac{1}{2}\,\text{tr}(\mathrm{D}f) \pm \{(\tfrac{1}{2}\,\text{tr}(\mathrm{D}f))^2 - 1\}^{\frac{1}{2}}.$$

For the periodic point at the origin we find

$$\text{tr}(\mathrm{D}f) = \alpha + 1/\alpha > 2,$$

and for the remaining periodic points

$$\text{tr}(\mathrm{D}f) = 2 + g(\alpha)(r^* - 1),$$

where

$$g(\alpha) = (\alpha - 1/\alpha)\tan^{-1}\{\tfrac{1}{2}(\alpha - 1/\alpha)\}.$$

Putting $G = \mathrm{tr}\,(\mathrm{D}f) - 2$, the eigenvalues and thus the character of the periodic points can be specified in terms of G as follows:

$G > 0$,	$\lvert\lambda_1\rvert > 1$, $\lvert\lambda_2\rvert < 1$	hyperbolic,
$G = 0$,	$\lambda_1, \lambda_2 = 1$	parabolic,
$0 > G > -4$,	λ_1, λ_2 complex, with $\lvert\lambda_1\rvert, \lvert\lambda_2\rvert = 1$	elliptic,
$G = -4$,	$\lambda_1, \lambda_2 = -1$	parabolic,
$-4 > G$,	$\lvert\lambda_1\rvert > 1$, $\lvert\lambda_2\rvert < 1$	hyperbolic.

(The residue of Greene (1979) is $-\frac{1}{4}G$.) Based on the above analysis, we can now infer the bifurcations that take place as β is increased from 0 for a fixed value of α.

When β is less than 1, there is only one periodic point at the origin that remains hyperbolic. At $\beta = 1$ two period-1 periodic points are formed at $r^* = 1$ as shown earlier. Both points are parabolic since $G = 0$ in this case. When β is increased to values greater than 1, each periodic point at r^* splits into two; the two at a radial distance of $r^* > 1$ are hyperbolic, while those at $r^* < 1$ are initially elliptic. Thus $\beta = 1, r^* = 1$ is a bifurcation value at which a 'saddle-node' bifurcation (Guckenheimer & Holmes 1983, p. 146) takes place. In a saddle-node bifurcation for area-preserving systems, as the parameter is increased the flow goes from no periodic points to one parabolic periodic point to two periodic points, one hyperbolic and one elliptic. As β is increased further, the inner periodic point, which is initially elliptic, moves closer to the origin and G becomes more negative. If $g(\alpha) > 4$, for β large enough $G = -4$ and a second bifurcation takes place in which the elliptic point becomes parabolic and then hyperbolic with increasing β. This bifurcation is known as a 'flip' bifurcation or 'period-doubling' bifurcation (Guckenheimer & Holmes 1983, p. 157), and in addition to the change in character of the period-1 periodic point, two elliptic period-2 periodic points are formed in the neighbourhood of the period-1 periodic point. The flip bifurcation is characterized by eigenvalues of value -1.

Assuming that α and β are large enough that the period-2 points exist, the following relations hold:

$$f(r_1^*, \theta_1^*) = (r_2^*, \theta_2^*), \quad f(r_2^*, \theta_2^*) = (r_1^*, \theta_1^*),$$

where (r_1^*, θ_1^*) and (r_2^*, θ_2^*) are the two period-2 periodic points formed near (r^*, θ^*). By symmetry, we can easily obtain the results for the period-2 periodic points near $(r^*, \theta^* + \pi)$. The eigenvalues depend on $\mathrm{tr}\,(\mathrm{D}f^2)$ where $\mathrm{D}f^2$ is the Jacobian of the mapping iterated twice. For period-2 points we have $x_1 \to x_2 \to x_1$, or

$$x_1 = f^2(x_1) = f(x_2),$$

and thus the Jacobian evaluated at the periodic points can be written as

$$\mathrm{D}f^2(x_1) = \mathrm{D}f(x_2)\,\mathrm{D}f(x_1), \quad \mathrm{D}f^2(x_2) = \mathrm{D}f(x_1)\,\mathrm{D}f(x_2),$$

where $\mathrm{D}f$ is the Jacobian of the mapping.

For the TW map, on simplification we obtain

$$\begin{aligned}\mathrm{tr}\,(\mathrm{D}f(x_2)\,\mathrm{D}f(x_1)) &= 2 + G_1 G_2 + 2(G_1 + G_2) \\ &\overset{\text{def}}{=} 2 + G',\end{aligned}$$

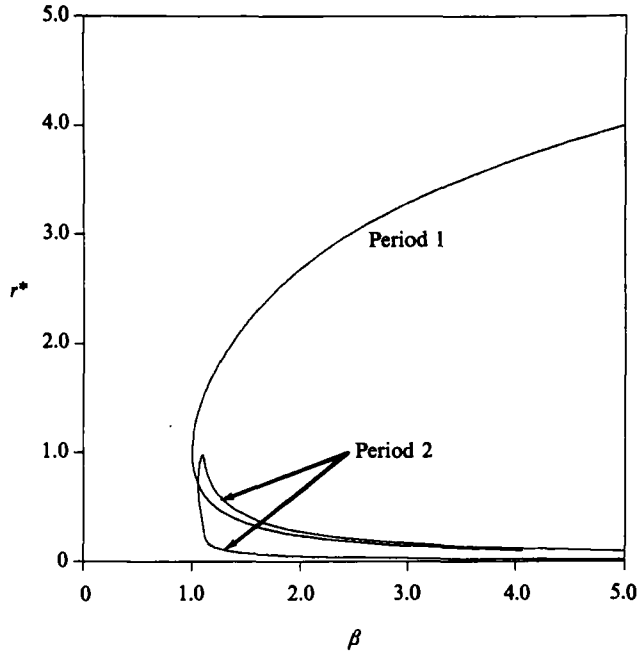

FIGURE 1. Radial position (r^*) of period-1 and period-2 periodic points of the TW mapping versus β. $\alpha = 10.0$.

where

$$G_1 = \frac{(2\theta_1^* - \frac{1}{2}\pi)(\alpha^4 - 1)(1 - r_1^*)}{\alpha_1(\alpha_2^2 + 1)}, \quad G_2 = \frac{(2\theta_2^* - \frac{1}{2}\pi)(\alpha^4 - 1)(1 - r_2^*)}{\alpha_2(\alpha_1^2 + 1)}.$$

and $\alpha_i = 1/\tan\theta_i^*, i = 1, 2$. At the birth of the period-2 periodic points $r_1^* = r_2^* = r^*, \alpha_1 = \alpha_2 = \alpha$ so that $G_1 = G_2 = G$, and

$$G' = G^2 + 4G.$$

At the flip bifurcation $G = -4$, which implies that $G' = 0$ so that the period-2 points are parabolic at the point of their formation. For slightly larger values of β we find that $G' < 0$ and period-2 periodic points become elliptic. As β is increased further, depending on the value of α, a second flip bifurcation may occur in which the period-2 points become hyperbolic and two period-4 elliptic points are formed for each period-2 point. At the bifurcation point $G' = -4$ so that we obtain

$$(G_1 + 2)(G_2 + 2) = 0.$$

In figure 1 we have plotted the radial position of period-1 and period-2 periodic points versus β for a fixed value of α. The character of the period-1 and period-2 periodic points, which are initially elliptic, can be inferred from figure 2 where we have plotted G and G' versus β for the case of figure 1. As β is increased the elliptic period-1 periodic point undergoes a flip bifurcation ($G < -4$), and a pair of elliptic period-2 periodic points are formed which subsequently undergo a flip bifurcation. Further increase in β results in a reverse flip bifurcation in which the period-2 hyperbolic points become elliptic and the period-4 points formed after the flip bifurcation coalesce with the period-2 points; this is followed by another flip bifurcation.

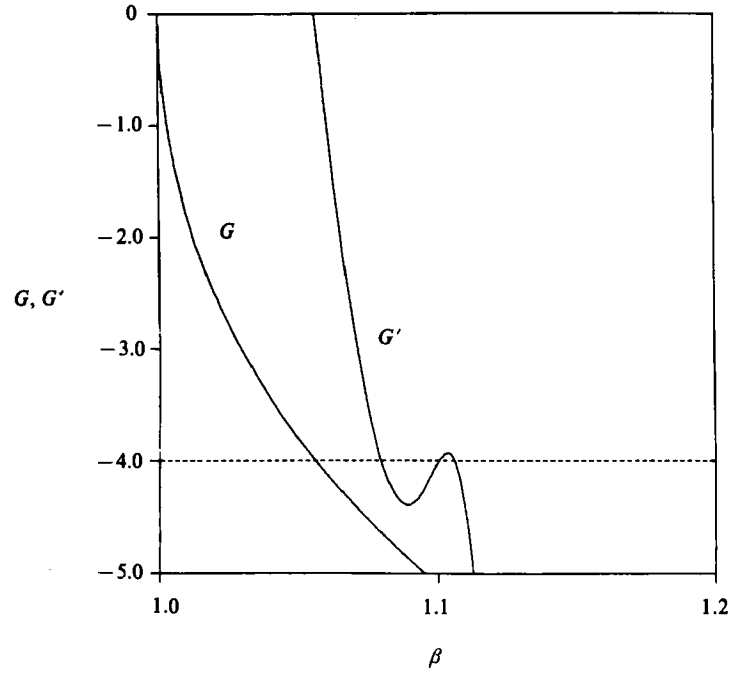

FIGURE 2. G and G' (see text) for the period-1 periodic points at $r^* < 1$, and the corresponding period-2 periodic points versus β for the TW mapping. $\alpha = 10.0$.

The behaviour of the period-1 and period-2 elliptic points is summarized in figure 3 where we have plotted flip-bifurcation values (i.e. the value of β at which the elliptic periodic point becomes hyperbolic) versus α for the period-1 and period-2 elliptic points. Figure 3(b) shows a magnified view of the region in which the behaviour described in figure 2 occurs. The dashed line in figure 3 corresponds to $\alpha = 10$. As is apparent from figure 3, the local bifurcations of the TW mapping are quite complex and do not exhibit a Feigenbaum universal cascade of period-doubling bifurcations as has been found for quadratic two-dimensional area-preserving mappings (Helleman 1980).

The existence of low-order elliptic points as shown above and the KAM surfaces surrounding them are of major importance from the point of view of mixing. When most of the KAM surfaces survive, the flow in an island around the elliptic periodic point is mostly regular and isolated from the rest of the fluid so that the mixing is poor. The flip bifurcation results in the breakup of the islands into smaller ones, though more higher-period islands are formed at each period doubling. The size of such islands is limited by the manifolds of the hyperbolic points, which also increase in number.

5. Global bifurcations of the tendril–whorl mapping

The stable and unstable manifolds of the period-1 periodic points provide us with the broad features of the flow which we utilize to qualitatively analyse the ability of the flow to mix. The main features of interest are regions or large-scale homoclinic behaviour in which we expect good mixing, and intersections between the manifolds of the different regions which can be interpreted as gates for transport between two

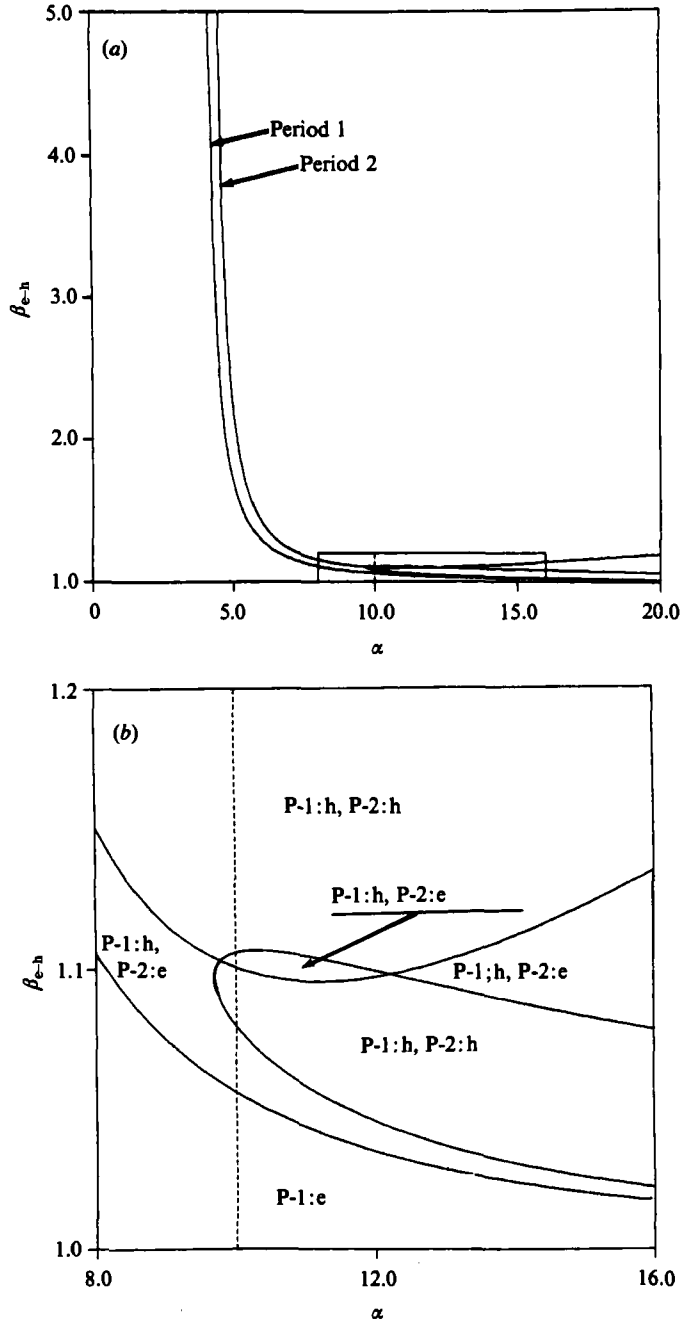

FIGURE 3. Flip-bifurcation values of β (value at which elliptic point becomes hyperbolic versus α for period-1 (P-1) and period-2 (P-2) points. (*b*) is a magnified view of box in (*a*). The dashed line corresponds to $\alpha = 10$.

homoclinic regions. We calculate the position of the manifolds numerically by surrounding each hyperbolic periodic point by a circle of small radius made up of a large number of points and convecting them by the flow. The unstable manifolds are found by mapping the points forward and the stable manifold by mapping them in reverse. The result is a thin filament (a line to the resolution of the graphics output

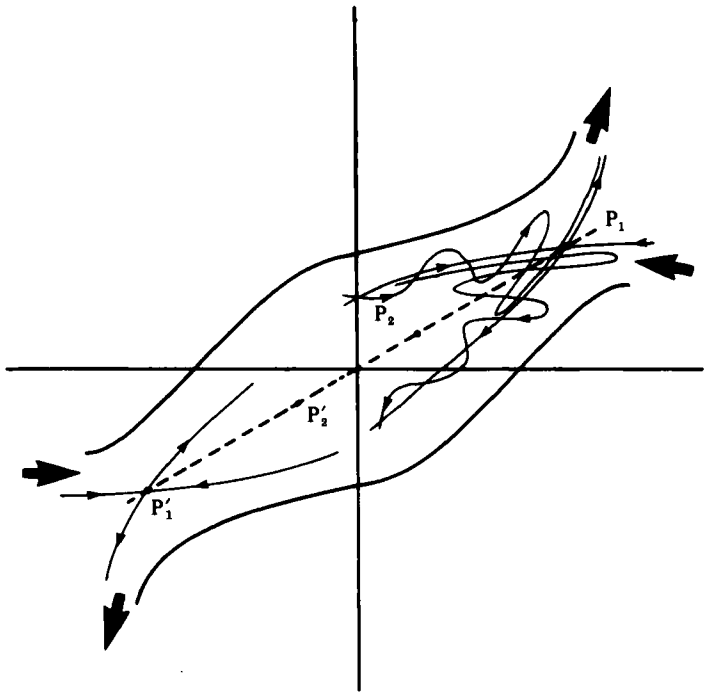

FIGURE 4. Schematic view of mixing zone. P_1 and P_1' are the outer period-1 periodic points, and P_2 and P_2' are the inner period-1 periodic points. Large arrows show the direction of transport through the conduits. The thickness of the conduits depends on the scale of heteroclinic behaviour near P_1 and P_1'.

device) which encases the manifold. Obviously, in the case of homoclinic behaviour, a larger portion of the infinitely long manifold is revealed with increasing numbers of mappings of the circle of points.

The flow produced by the TW mapping is for most part regular and looks like an extensional flow. The complicated behaviour, and thus the mixing, is confined to a well-defined region around the periodic points shown schematically in figure 4. The TW mapping can thus be considered to be a continuous mixing system in which material enters through conduits around the stable manifolds and leaves via conduits around the unstable manifolds of the outer period-1 periodic points (figure 4). The thickness of the conduits and the flux into the mixing zone depend largely on the scale of homoclinic behaviour near the periodic point. Below we present the results of calculations for different values of α to illustrate the global bifurcations of the flow as β is increased from 1.

Figure 5 shows the manifolds of the hyperbolic period-1 periodic points at $r^* > 1$ (P_1 and P_1') and at the origin (O) for two different values of β for $\alpha = 1.5$. The manifolds seem to join smoothly in both cases and the flow looks regular to the resolution of the graphics output device. At low values of β the manifolds of P_1 and P_1' intersect themselves while those of O are outside as shown in figure 5(a). At a higher value of β, the manifolds of P_1 and P_1' intersect each other and envelope those of O which self-intersect as shown in figure 5(b). The bifurcation occurs at an intermediate value of β when the manifolds of O overlap those of P_1 and P_1'. The mixing is poor in this case as the conduits are infinitesimally small and the heteroclinic behaviour is also confined to a very small scale.

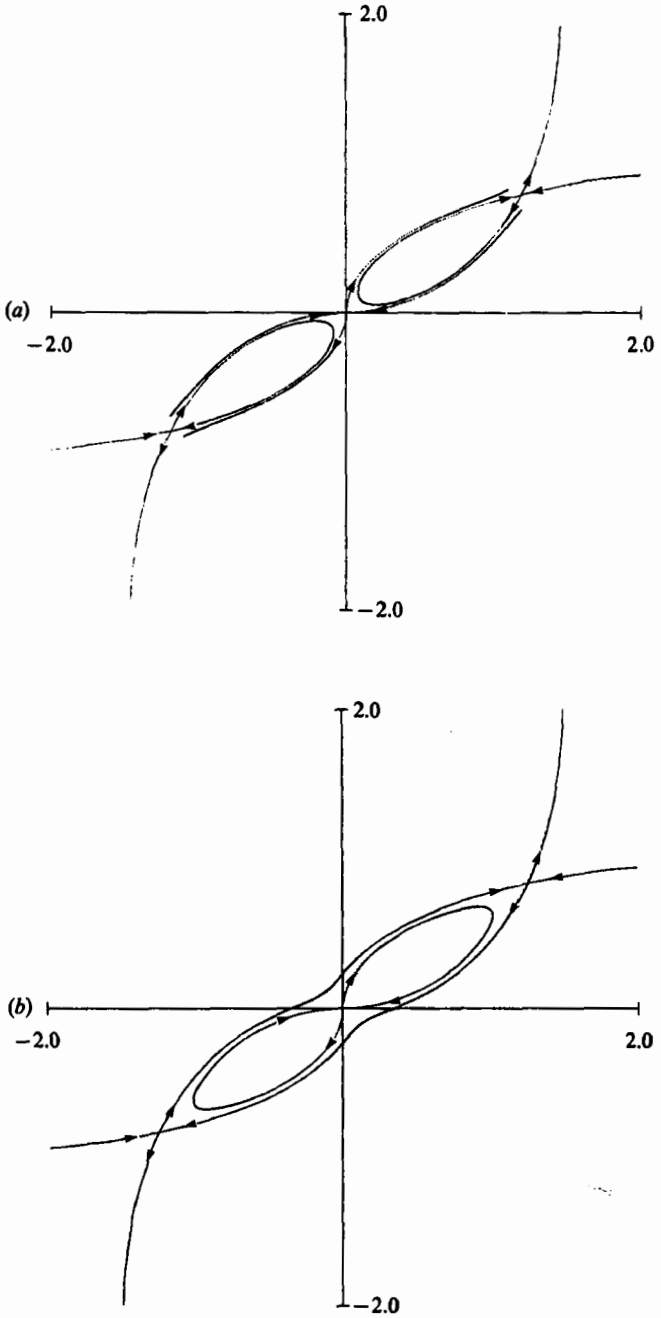

FIGURE 5. Stable and unstable manifolds of P_1 and P_1' and O for $\alpha = 1.5$; (*a*) before the bifurcation, $\beta = 1.075$; (*b*) after the bifurcation, $\beta = 1.099$.

Figure 6 shows the manifolds of P_1, P_1', and O for a larger value of α ($\alpha = 5$) and increasing values of β. The bifurcation that takes place is similar to that described above where the manifolds of the origin overlap with those of P_1 and P_1' as β is increased and are finally enveloped by them as can be seen from figure 6(*a–c*). The homoclinic and heteroclinic behaviour is clearly evident in this case. In figure 6(*c*)

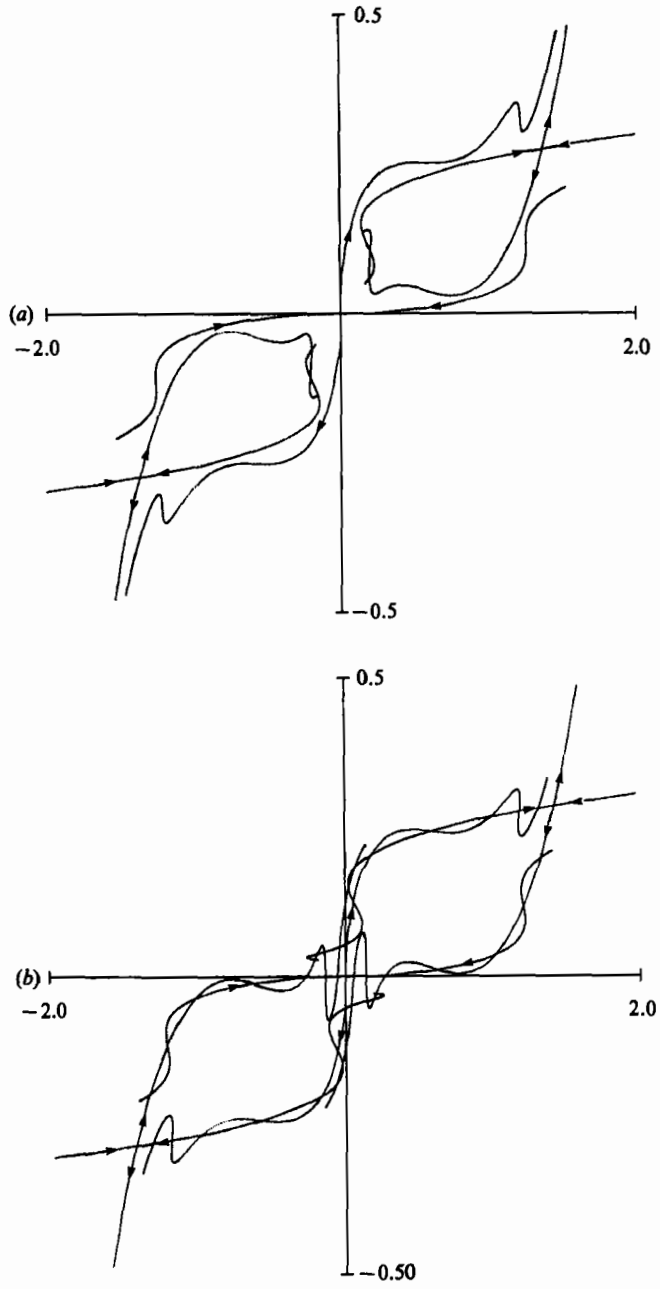

FIGURE 6(a, b). For caption see facing page.

though the manifolds of O are not shown to intersect with those of P_1 and P_1', in fact they do as would be revealed if a larger portion of the manifolds were drawn. Based on the large-scale homoclinic behaviour we expect the conduits to be of large size resulting in flux into the mixing zone. Prior to the intersection between the manifolds of the origin and the outer periodic points (figure 6*a*), the mixing zone is divided into two compartments that are isolated from each other; the intersection of the manifolds opens up channels of transport from one compartment to the other. The KAM

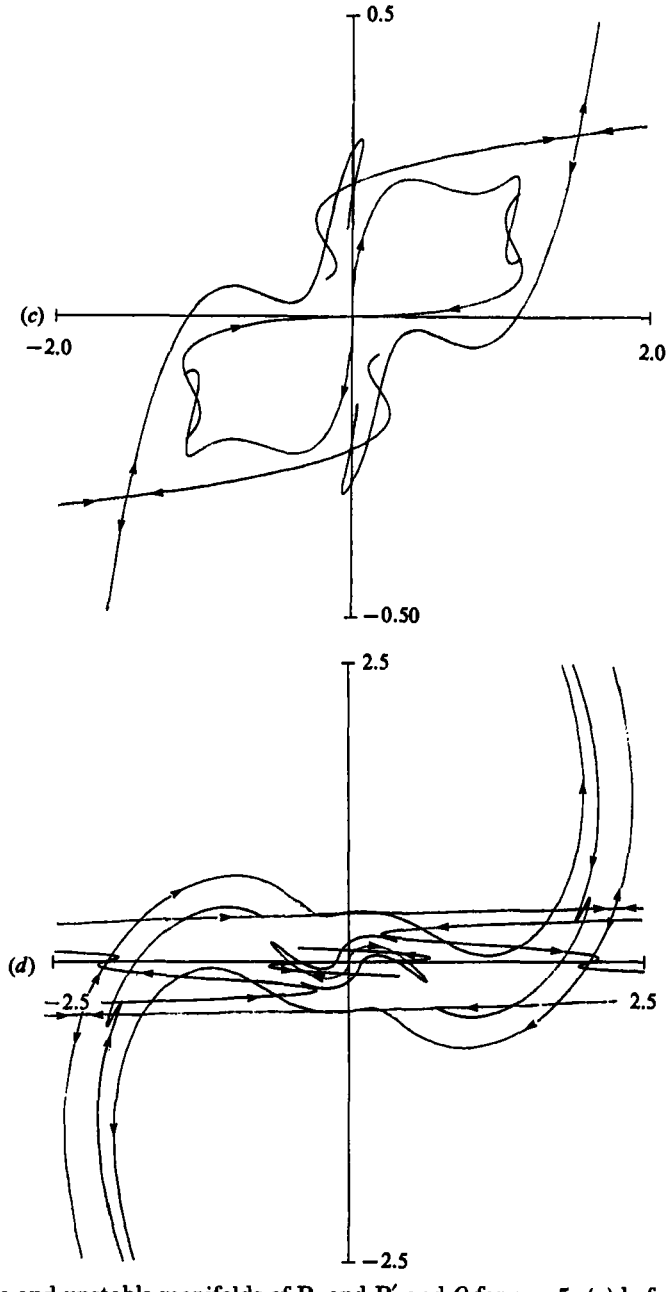

FIGURE 6. Stable and unstable manifolds of P_1 and P_1' and O for $\alpha = 5$; (*a*) before the bifurcation, $\beta = 1.066$; (*b*), (*c*) after the bifurcation, $\beta = 1.082$ and 1.118 respectively. (*d*) Wild behaviour of the manifolds reduces size of the island around the elliptic period-1 periodic point, $\beta = 1.595$. Note change in scale.

surfaces around each elliptic point result in islands inside the mixing zone, the largest being those of the period-1 periodic points (P_2 and P_2'). The size of the islands is determined by the KAM surface furthest from the elliptic point that still survives and thus depends on the scale of the homoclinic/heteroclinic behaviour of the surrounding manifolds. In figure 6 (*d*) we show the manifolds at larger-value β when

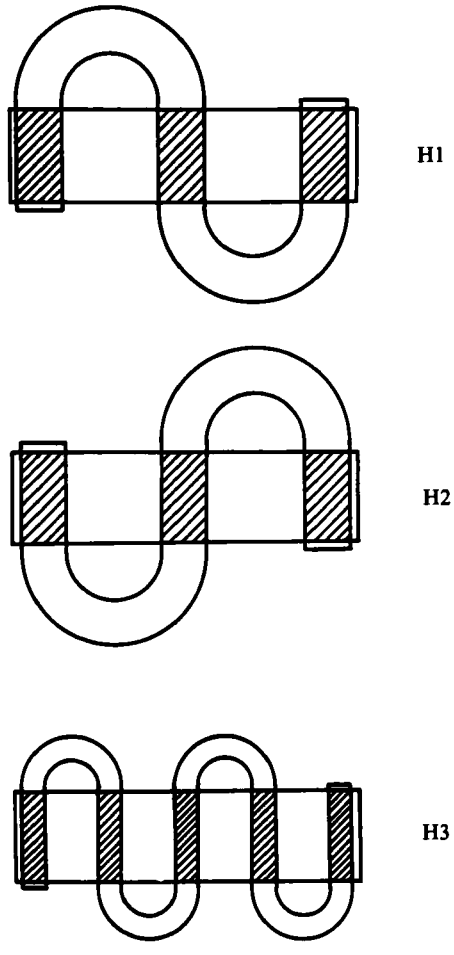

FIGURE 7. Schematic view of the three types of period-1 horseshoes possible for the TW mapping.

the size of the islands around P_2 and P_2' is greatly reduced by the large-scale heteroclinic behaviour. The mixing in this case is expected to be good.

From the above analysis we see that when α is small the flow is almost regular and the mixing is poor for all β. As α is increased the scale of homoclinic behaviour increases and for a large enough value of β there are intersections between the manifolds of the outer periodic points and those of the origin resulting in a single connected mixing zone. The mixing zone is not homogeneous, and is expected to contain islands of regular flow around each elliptic periodic point, the largest islands being around the period-1 periodic points. As shown above, the size of the islands decreases with increasing α and β. When α is large enough, the islands also breakup into smaller ones of higher period due to the flip bifurcation.

A homoclinic intersection implies the existence of a horseshoe set (Smale–Birkhoff Homoclinic Theorem, Guckenheimer & Holmes 1983, p. 252); however, such horseshoes may be of period higher than 1. Horseshoes of period-1, besides being easier to study, also result in the most rapid mixing. We show the existence of period-1 horseshoes by the following construction. We choose a rectangle centred at the origin whose forward image intersected with itself results in 'vertical' strips. When the sides

of the rectangle are chosen in the ratio $\alpha:1$ with the longer side parallel to the x-axis, if the forward image intersects properly with the rectangle, the inverse image also does so resulting in 'horizontal' strips. This is easily seen from the fact that the rectangle is mapped by the extensional flow to another rectangle whose sides are in the same ratio ($\alpha:1$), this time with the longer side parallel to the y-axis, so that the 'horizontal' strips are mapped into the 'vertical' strips.

In the case of the TW mapping we find that 3 different types of period-1 horseshoes may be formed depending on the value of α for β large enough, as shown in figure 7. (Whereas the existence of any type of horseshoe is indicative of chaos the various types have different implications for fluid mixing.) In figure 8(*a*) we show a horseshoe of type H1 for a value of $\alpha = 5$. For a larger value of α ($\alpha = 10$) we obtain overlapping horseshoes, one of type H1 (figure 8*b*) and one of type H2 (figure 8*c*). Finally at an even larger value of α ($\alpha = 25$) we obtain a horseshoe of type H3 as shown in figure 8(*d*). In all the above cases the conditions of horizontality and verticality required by Moser's construction (Guckenheimer & Holmes 1983, p. 241) are easily satisfied thus implying the existence of an invariant Cantor set Λ of isolated points which remain inside the rectangle for all time. The set Λ is contained in the rectangles formed by the intersection of the vertical and horizontal strips and contains points that are periodic with arbitrarily long periods as well as points that exhibit bounded aperiodic motion. The most rapid mixing takes place in the neighbourhood of Λ; however, the existence of higher-order horseshoes which overlap the period-1 horseshoes results in a larger mixing zone. An implication of practical significance of the above result is that good mixing occurs in the neighbourhood of the origin well below the lengthscale at which the velocity fields may be approximated to be linear.

6. The Aref-blinking-vortex flow

This flow is generated by two point vortices separated by a periodic distance that blink on and off periodically in an unbounded fluid. At any given time only one of the vortices is on so that the motion during each period is made up of two consecutive rotations about different centres. The flow was proposed as an idealized model of a stirred tank (Aref 1984). As was pointed out by Aref & Tryggvason (1984) the velocity field due to the vortex can be realized approximately by a circular cylinder spinning in a large pool of a viscous liquid. The flow also turns out to be qualitatively similar to a periodically operated cavity flow (Chien, Rising & Ottino 1986) which has been studied experimentally, and can be regarded as a special case of a more general class of flows with non-constant speed on streamlines (Rising 1986). The distinguishing feature of the flow, however, is that it is composed of a sequence of 'weak' flows, in which the lengths of material lines increase linearly with time, and yet is able to mix well as we show below. Such bounded flows also have the property of an 'optimum' operating condition at which the average stretching efficiency is maximized as we demonstrate for the BV flow.

The velocity field due to a single point vortex at the origin is given by

$$v_r = 0, \quad v_\theta = \frac{\Gamma}{2\pi r},$$

where Γ is the strength of the vortex. The above velocity field can easily be integrated over the time T during which the vortex exists to give the following mapping

$$g\colon (r,\theta) \to (r, \theta + \Delta\theta)$$

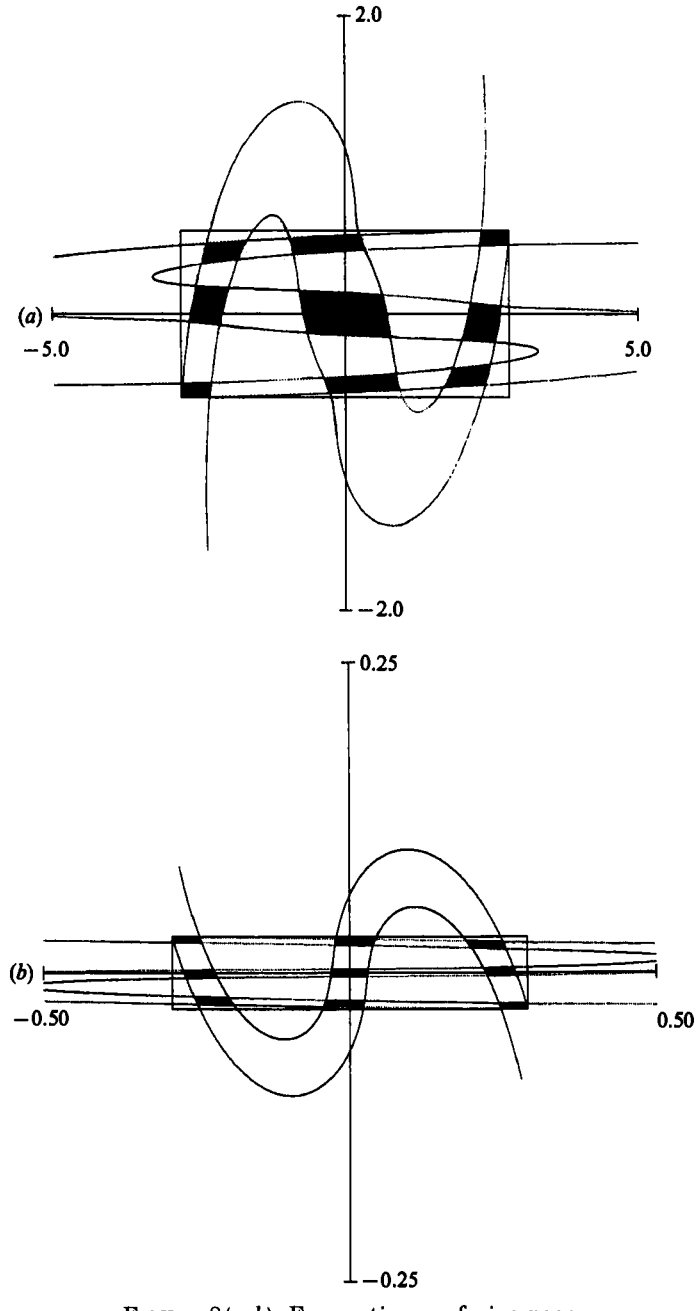

FIGURE 8(a, b). For caption see facing page.

where $\Delta\theta = \Gamma T/2\pi r^2$. Taking the vortices to be at $(-a, 0)$ and $(a, 0)$ in a Cartesian co-ordinate system, the mapping in dimensionless form is given by

$$f_\xi\colon (x, y) \to (\xi + (x-\xi)\cos\Delta\theta - y\sin\Delta\theta,\ (x-\xi)\sin\Delta\theta + y\cos\Delta\theta),$$

where ξ is the position of the vortex, $\Delta\theta = \mu/r^2$, and

$$r = ((x-\xi)^2 + y^2)^{\frac{1}{2}}.$$

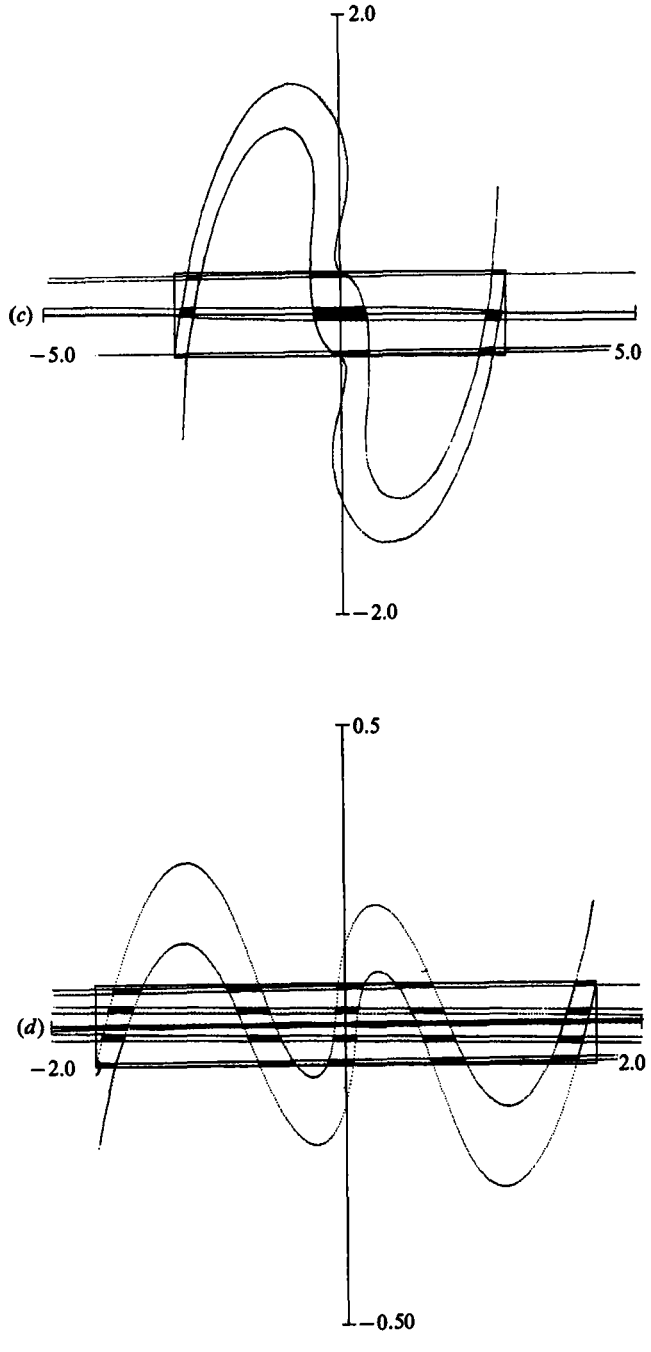

FIGURE 8. Construction of period-1 horseshoes for the TW mapping. The forward image of the rectangle intersected with itself gives 'vertical' strips, and the inverse image of the rectangle intersected with itself gives 'horizontal' strips. The invariant set Λ is contained in the shaded regions which are the intersection of the vertical and horizontal strips. (*a*) For $\alpha = 5, \beta = 2.239$, we obtain a horseshoe of type H1. For $\alpha = 10, \beta = 2.180$, we obtain overlapping horseshoes of type H1 (*b*), and H2 (*c*). (*d*) For $\alpha = 25, \beta = 1.185$, we obtain a horseshoe of type H3.

In the above equations distances are made dimensionless with respect to a so that the vortices are at $\xi = \pm 1$, and the dimensionless flow strength μ is defined as

$$\mu = \Gamma T/2\pi a^2.$$

In the following analysis we assume that the vortex at $\xi = 1$ is switched on first and that the rotation is counterclockwise ($\mu > 0$).

The flow far from the vortices looks like a rotation about the origin and thus the motion of the fluid particles is bounded, in contrast to the TW mapping in which the flow is dominated by the extensional flow and particles are convected towards infinity. As shown by Aref (1984), at low flow strengths the motion appears to be mostly regular except in small regions around the vortices, and at higher flow strengths, chaotic, so that the single parameter of the system, μ, can be varied smoothly to go from a poor mixing system to a good mixing system.

7. Local bifurcations of the blinking-vortex mapping

Since each period of the flow is made up of two consecutive rotations, if (x^*, y^*) is a period-1 periodic point then

$$f_{+1}(x^*, y^*) = (x^*, -y^*) \quad \text{and} \quad f_{-1}(x^*, -y^*) = (x^*, y^*),$$

as can be seen from figure 9. Denoting the distances of the periodic point from the vortices as R_1 and R_2, and the semi-angles subtended at the vortices by the line segment joining (x^*, y^*) and $(x^*, -y^*)$ as θ_1 and θ_2 (see figure 9), the equations for the periodic points are given by

$$R_1 \cos\theta_1 + R_2 \cos\theta_2 = 2, \quad R_1 \sin\theta_1 = R_2 \sin\theta_2,$$

where

$$\theta_i = \tfrac{1}{2}(\Delta\theta(R_1) - 2\pi n_i) \quad (i = 1, 2) \quad \text{for } y^* > 0,$$

and

$$\theta_i = \pi - \tfrac{1}{2}(\Delta\theta(R_i) - 2\pi n_i) \quad (i = 1, 2) \quad \text{for } y^* < 0.$$

In the above equations n_i is the number of full rotations about the corresponding vortex and is given by

$$n_i = \text{Integer}\left(\frac{\Delta\theta(R_i)}{2\pi}\right) \quad (i = 1, 2).$$

There are multiple solutions to the above nonlinear equations for a given flow strength, and we visualize the position of all the period-1 periodic points by the following graphical construction. We put

$$x_1(s_1) = 1 - s_1 \cos\theta_1, \quad y_1(s_1) = s_1 \sin\theta_1,$$
$$x_2(s_2) = 1 + s_2 \cos\theta_2, \quad y_2(s_2) = s_2 \sin\theta_2,$$

where $\theta_i = \theta(s_1)$ as above, so that when $x_1 = x_2$ and $y_1 = y_2$, the equations for the periodic point are satisfied with $s_1 = R_1$ and $s_2 = R_2$. In figure 10 we plot the graphs of x_i versus y_i and x_i versus $-y_i$ $(i = 1, 2)$ for different values of the flow strength. The points of intersection between the graphs are then the periodic points. As may be expected from the definition of θ_i, the graphs are discontinuous and we label each segment of the graph by n_i, the number of rotations about the vortex. At low values of μ (figure 10*a*), there are a number of periodic points all of which lie above the x-axis, and are formed by the intersection of the segments $n_i = 0$ with $n_j \geqslant 0$. As the flow strength is increased all but three of the periodic points disappear (figure 10*b*), and

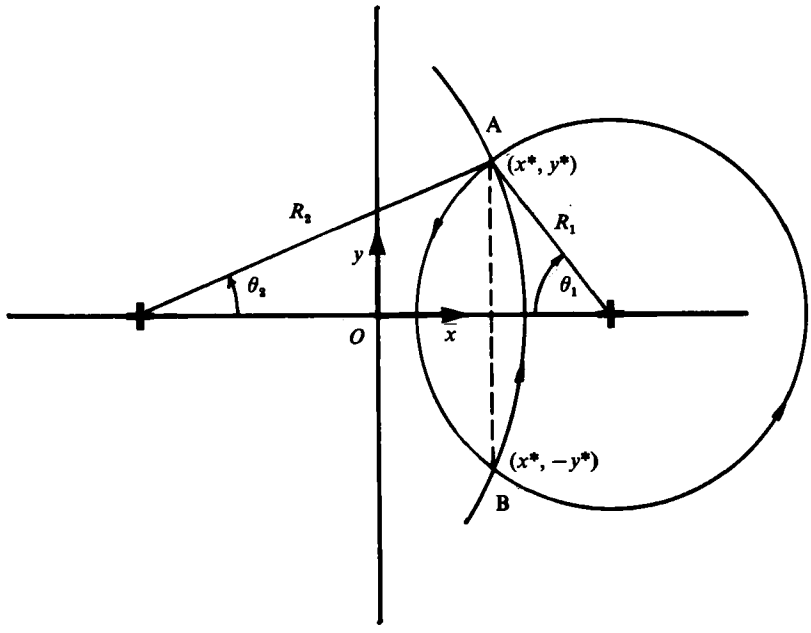

FIGURE 9. Location of a period-1 periodic point (x^*, y^*) and its image after a half-cycle of the flow $(x^*, -y^*)$ relative to the vortices (+) for the BV mapping. R_1 and R_2 are the distances of both (x^*, y^*) and $(x^*, -y^*)$ from the right and left vortices respectively. $2\theta_1$ and $2\theta_2$ are the angles subtended by AB at right and left vortices respectively.

at high flow strengths (figure 10*c*) there are again a number of periodic points, some of which lie below the x-axis.

The character of the period-1 points depend on $\mathrm{tr}\,(\mathrm{D}\boldsymbol{f})$, where $\boldsymbol{f}$ is the mapping composed of the two rotations

$$\boldsymbol{f} = \boldsymbol{f}_{-1} \cdot \boldsymbol{f}_{+1}.$$

As before we put

$$\mathrm{D}\boldsymbol{f}(x^*, y^*) = \mathrm{D}\boldsymbol{f}_{-1}(x^*, -y^*)\,\mathrm{D}\boldsymbol{f}_{+1}(x^*, y^*)$$

and on simplification obtain

$$\mathrm{tr}\,(\mathrm{D}\boldsymbol{f}(x^*, y^*)) = 2 + 4\sin(\theta_1+\theta_2)\{(\Delta\theta_1\,\Delta\theta_2 - 1)\sin(\theta_1+\theta_2) + (\Delta\theta_1 + \Delta\theta_2)\cos(\theta_1+\theta_2)\}$$
$$\overset{\text{def}}{=} 2 + G,$$

where θ_i and $\Delta\theta_i$ are as defined earlier.

By considering the relative slopes of the lines in the graphical construction at the intersection points we can infer that each time two segments of the graphs (x_t, y_t) and $(x_t, -y_t)$ are tangent to one another, a saddle-node bifurcation occurs in which the period point is initially parabolic, and on decreasing μ splits into two period-1 periodic points, one of which is hyperbolic, the other elliptic. Of the periodic points formed by the intersection of $n_t = 0$, and $n_j > 0$ and the x-axis, the one closer to the origin is hyperbolic, and the other elliptic. Of the periodic points formed at high flow strengths (figure 10*c*), the upper periodic points are hyperbolic and the lower ones elliptic. Further change in μ may result in a flip bifurcation for the elliptic points if G becomes sufficiently negative ($G < -4$).

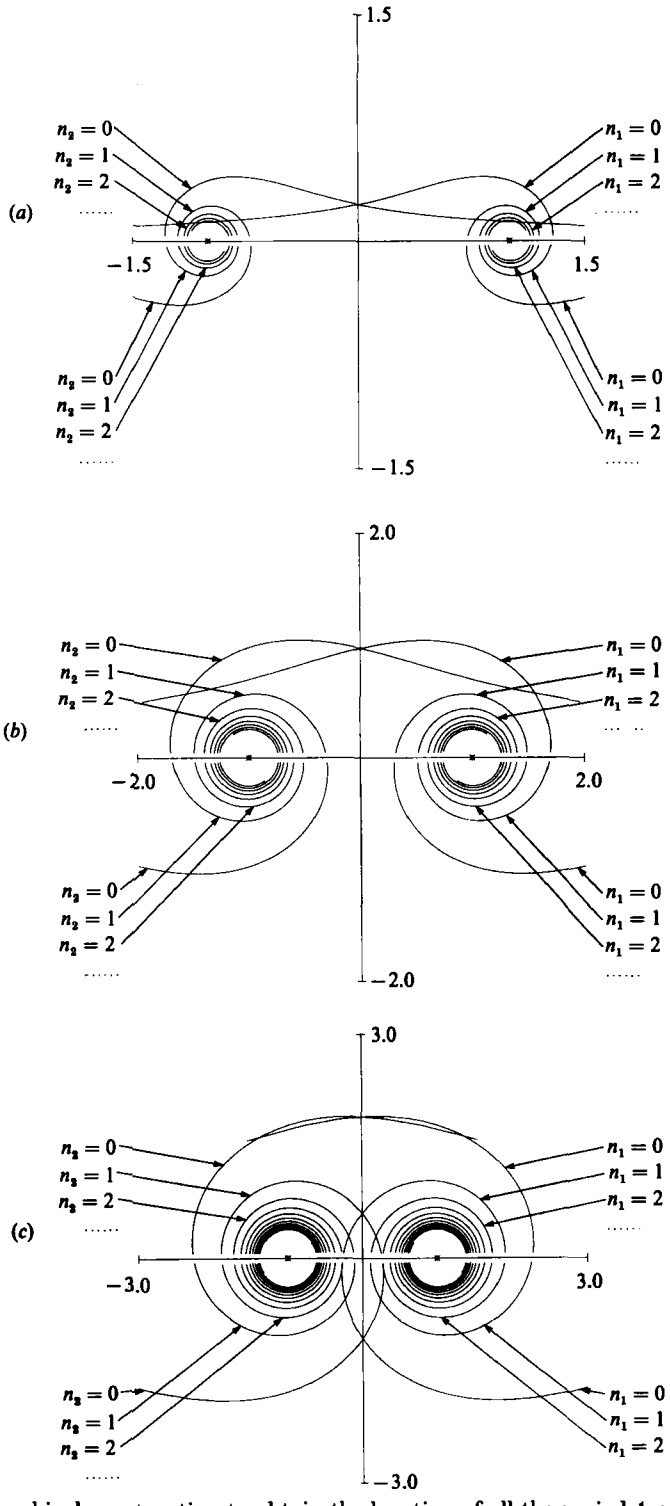

FIGURE 10. Graphical construction to obtain the location of all the period-1 periodic points of the BV mapping for different flow strengths μ. The periodic points are at the intersection points of the segments of the graphs $(x_1, \pm y_1)$, labelled n_1, with the segments of the graphs $(x_2, \pm y_2)$, labelled n_2. (*a*) $\mu = 0.5$; (*b*) 3.0; (*c*) 10.0.

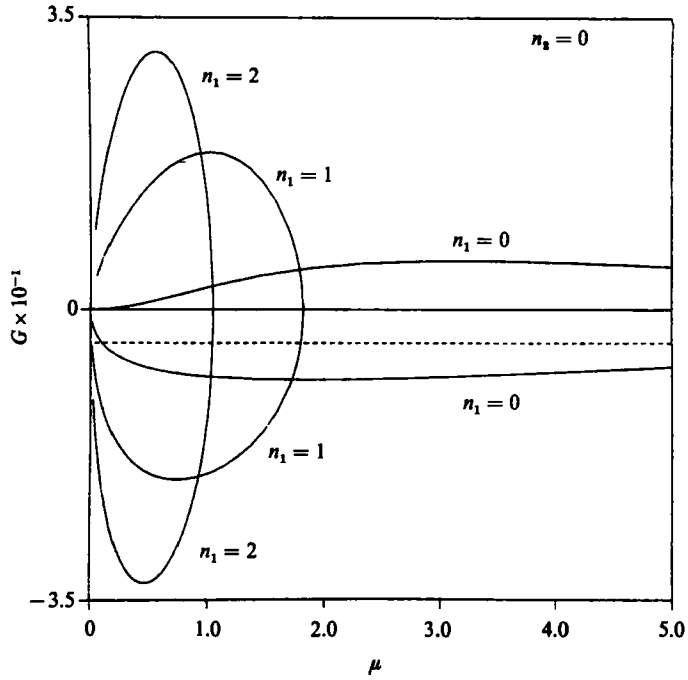

FIGURE 11. G (see text for definition) for different period-1 periodic points versus the flow strength μ for the BV mapping. The graph for each pair of periodic points is labelled by the segment n_1 of the graph (x_1, y_1) that intersects with segment $n_2 = 0$ of graph (x_2, y_2) (see figure 10) to form the periodic points. The outer periodic points have $G < 0$, and the inner periodic points have $G > 0$. The dashed line corresponds to $G = -4$. The graphs are identical for the symmetric period-1 periodic points in the left half-plane.

In figure 11 we plot the calculated value of G versus μ for the periodic points formed by the intersection of the segment $n_2 = 0$ with the segments $n_1 = 0$, $n_1 = 1$, and $n_1 = 2$ for $y^* > 0$. The graphs for the inner periodic points lie above the G-axis while those of the outer periodic points lie below the G-axis, as expected from the above considerations. The dashed line in figure 11 corresponds to $G = -4$ at which the flip bifurcation takes place.

8. Global bifurcations of the blinking-vortex mapping

The Poincaré sections obtained by Aref (1984) showed that at low values of μ the flow seems to be regular except in small regions around each vortex. As μ was increased the chaotic regions around the vortices increased in size, and a third chaotic region in the shape of a figure-of-eight became apparent. Finally, at a high enough value of μ, the chaotic region around each vortex overlapped with the figure-of-eight region forming a single connected chaotic region.

The above behaviour can be explained by studying the interactions of the manifolds of the period-1 periodic points formed by the intersections of the segments $n_1 = 0$ and $n_2 = 0$ (figure 10). Though the outer periodic points are elliptic at the point of formation, they are hyperbolic for the range of μ over which we carry out the calculations (figure 11). Figure 12 shows the stable and unstable manifolds of the periodic points specified above for a series of increasing flow strengths; the manifolds of the outer periodic point in the left half-plane are not drawn and may be inferred by

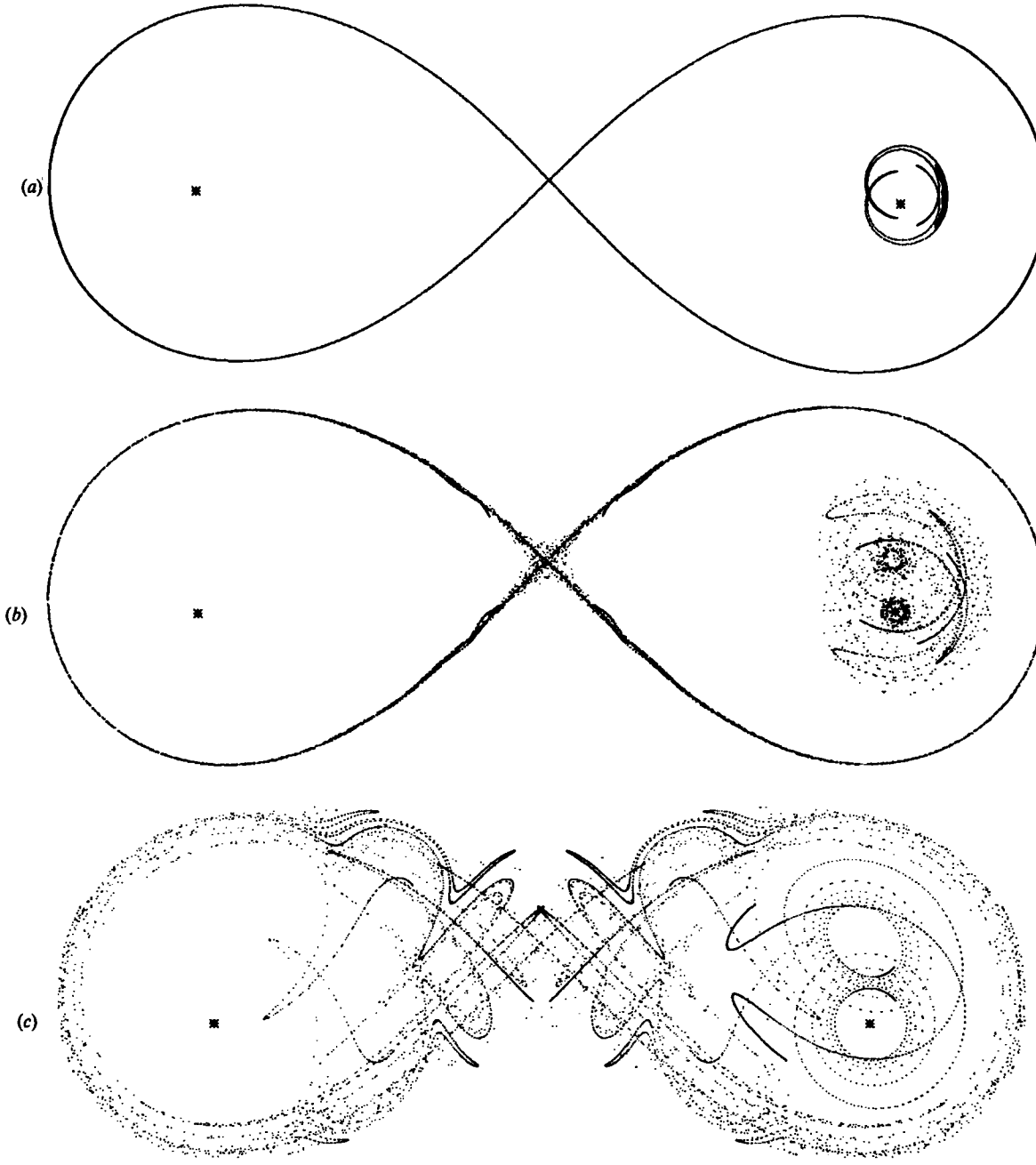

FIGURE 12. Stable and unstable manifolds of period-1 periodic points formed by the intersection of the segments $n_1 = 0$ and $n_2 = 0$ of the BV mapping for different flow strengths μ. (*a*) $\mu = 0.1$, (*b*) 0.3, and (*c*) 0.5. (Manifolds of the symmetric periodic point in the left half-plane are not drawn.)

symmetry. For low flow strengths (figure 12*a*) the manifolds of the central periodic point seem to join smoothly, and the homoclinic behaviour occurs at a lengthscale below the resolution of the graphics device; the homoclinic behaviour of the manifolds of the outer periodic points, however, is clearly apparent in this case. At higher values of the flow strength (figure 12*b*), the homoclinic behaviour of the

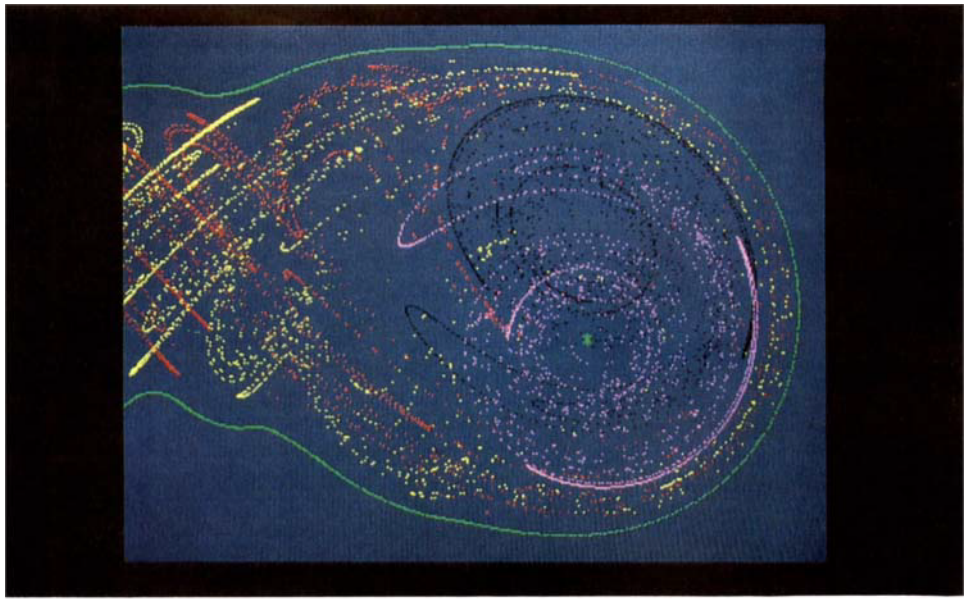

(a)

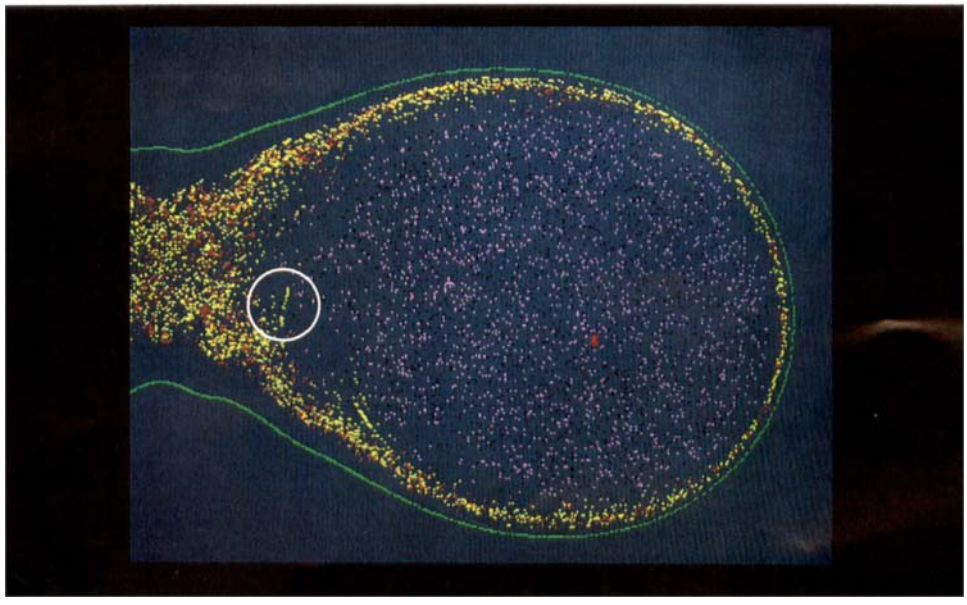

(b)

FIGURE 13. Magnified view of the stable and unstable manifolds of period–1 periodic points formed by the intersection of the segments $n_1 = 0$ and $n_2 = 0$ of the BV mapping for two different flow strengths *(a)* $\mu = 0.5$, *(b)* $\mu = 0.38$. Each manifold is a different colour: manifolds of the central periodic points are red–unstable, yellow–stable; manifolds of the outer periodic points are black–unstable, pink–stable. The green boundary is a KAM curve and an asterix denotes the position of a vortex. Manifolds do not appear continuous in *(b)* due to the large number of iterations. Note transverse intersection between manifolds of the outer and central periodic points in the encircled region in *(b)* (yellow and black).

manifolds of the central periodic point becomes evident, while that of the outer periodic points increases in scale. At large values of μ (figure 12*c*), the manifolds overlap forming a single 'globally chaotic' region.

The global bifurcation occurs at an intermediate flow strength ($\mu = 0.36$) when the last of the KAM surfaces separating the figure-of-eight region from each chaotic region around each vortex is destroyed and the outer manifolds intersect with the central one. The above bifurcation is often referred to as the 'transition to global chaos' (Greene 1979). Figure 13 (plate 1) shows a magnified view of the manifolds at a flow strength close to the bifurcation value (figure 13*b*), and at a higher flow strength (figure 13*a*), each manifold being a different colour. In figure 13(*b*), the manifolds do not appear as a continuous line owing to the large number of iterations. As a result, the intersections between the manifolds of the outer and central periodic points are only barely evident in this case (encircled region in figure 13*b*).

A single heteroclinic intersection as above implies an infinite number of such intersections and the original KAM surface is infinitely perforated but does not disappear entirely. The intersections act as gates for transport between the two homoclinic regions, and the remnant of the last surviving KAM surface or 'cantorus' (MacKay, Meiss & Percival 1984) acts as a leaky barrier to transport from one region to the other for μ close to the bifurcation value, as we show below.

9. Stretching of material lines, Liapunov exponents and average efficiency

Material lines stretch at an exponential rate on the average in the chaotic region, thus accurate computations of the length of a material line can be carried out for relatively few cycles of the flow. Also the rate of stretching is non-uniform and depends on the initial condition so that such calculations are useful mainly for qualitative considerations. A convenient measure for quantifying the local stretching of material lines on the average is the Liapunov exponent, defined as

$$\sigma(\boldsymbol{x}_0, \hat{\boldsymbol{m}}) = \lim_{t\to\infty} \frac{1}{t} \ln |\mathrm{D}\boldsymbol{f}_t(\boldsymbol{x}_0)\cdot\hat{\boldsymbol{m}}|$$

with respect to an initial position $\boldsymbol{x}_0$ and orientation $\hat{\boldsymbol{m}}$, where $\mathrm{D}\boldsymbol{f}_t$ is the Jacobian of the mapping at time t. (In the case of mappings t is replaced by n, the number of cycles.) Osledec (1968) has shown that for bounded, p-dimensional Hamiltonian flows, there exist p such exponents corresponding to a p-dimensional basis at $\boldsymbol{x}_0$ for almost all $\boldsymbol{x}_0$. Bennetin *et al.* (1980*a*) have proposed a method for calculating all the exponents taking into account the fact that the growth of small numerical errors results in the calculated value tending to the largest exponent for all initial conditions.

The Liapunov exponent can be physically interpreted as the long-time average of the 'specific stretching rate' ($\dot{\lambda}/\lambda$) as can be seen from the following formalism:

$$\begin{aligned}\lim_{t\to\infty} \frac{1}{t} \int_0^t \frac{\dot{\lambda}}{\lambda} \mathrm{d}t &= \lim_{t\to\infty} \frac{1}{t} \ln \lambda(\boldsymbol{x}_0, \hat{\boldsymbol{m}}, t), \\ &= \sigma(\boldsymbol{x}_0, \hat{\boldsymbol{m}})\end{aligned}$$

where $\lambda(\boldsymbol{x}_0, \hat{\boldsymbol{m}}, t) = |\mathrm{D}\boldsymbol{f}_t(\boldsymbol{x}_0)\cdot\hat{\boldsymbol{m}}|$. Based on the above interpretation, we define a second related quantity, the average stretching efficiency, as

$$\langle e(\boldsymbol{x}_0, \hat{\boldsymbol{m}})\rangle_\infty = \lim_{t\to\infty} \frac{1}{t} \int_0^t e(\boldsymbol{x}_0, \hat{\boldsymbol{m}}, t)\, \mathrm{d}t,$$

where the efficiency is defined as (Chella & Ottino 1985)

$$e(\boldsymbol{x}_0, \hat{\boldsymbol{m}}, t) \overset{\text{def}}{=} \frac{\boldsymbol{D} : \hat{\boldsymbol{m}}\hat{\boldsymbol{m}}}{(\boldsymbol{D} : \boldsymbol{D})^{\frac{1}{2}}}$$

$$= \frac{\dot{\lambda}/\lambda}{(\boldsymbol{D} : \boldsymbol{D})^{\frac{1}{2}}}$$

and $\boldsymbol{D}$ is the symmetric part of the velocity-gradient tensor. As can be seen from the equation above, the efficiency is simply a normalized stretching rate, the normalizing factor proportional to the square root of the rate of viscous dissipation in the case of Newtonian fluids. For two-dimensional area-preserving flows it can be shown that

$$|e| \leqslant 1/\sqrt{2},$$

the limits corresponding to a material element oriented along the direction of maximum stretching or maximum compression in a purely extensional flow. As shown by Chella & Ottino (1985), all linear flows with a velocity-gradient tensor whose eigenvalues are not purely imaginary, can be classified by their corresponding asymptotic efficiency. The average efficiency defined above classifies flows in the same sense, that is, two flows are considered to be identical if the average specific rate of stretching per rate of local energy dissipation is the same. Such a classification is useful from a practical viewpoint since the stretching and hence mixing is related to the energy supplied to the system. Thus the Liapunov exponent and the average efficiency together provide us with a description of the local stretching of material lines, the former specifying the average stretching rate, while the latter, the type of flow on the average.

The length stretch λ for mappings can be found analytically for each period as

$$\lambda_t = |\mathrm{D}\boldsymbol{f}(\boldsymbol{x}_i) \cdot \hat{\boldsymbol{m}}_i|,$$

where $\boldsymbol{x}_i = \boldsymbol{f}(\boldsymbol{x}_{i-1})$ and $\hat{\boldsymbol{m}}_i = \mathrm{D}\boldsymbol{f}(\boldsymbol{x}_{i-1}) \cdot \hat{\boldsymbol{m}}_{i-1}/\lambda_{i-1}$. Thus the largest Liapunov exponent can be computed iteratively using the above formulae to give

$$\sigma(\boldsymbol{x}_0, \hat{\boldsymbol{m}}_0) = \lim_{n \to \infty} \frac{1}{nT} \sum_{i=1}^{n} \ln \lambda_i.$$

In the case of the blinking-vortex flow, the magnitude of the rate of deformation tensor $\boldsymbol{D}$ is given by

$$(\boldsymbol{D} : \boldsymbol{D})^{\frac{1}{2}} = \sqrt{2}\frac{\mu}{r^2},$$

which is constant over each half-cycle. Thus the average efficiency is calculated by a similar procedure as for the Liapunov exponent outlined above.

The Liapunov exponent and average efficiency were calculated for large numbers of cycles of flow for the blinking-vortex system. Both quantities tend to positive limit values for points in the chaotic region, the limit values being almost independent of the initial location and orientation of the material element in the chaotic region. Positive Liapunov exponents imply that material lines stretch at an exponential rate on the average leading to good mixing. We caution, however, that a number of problems arising from the finite precision of the computation remain to be addressed rigorously in the calculation of long-time averages as was pointed out by Bennetin *et al.* (1980*b*). When the motion is sufficiently chaotic and the numerical precision sufficiently high the time averages are expected to be reliable (Bennetin *et al.* 1980*b*).

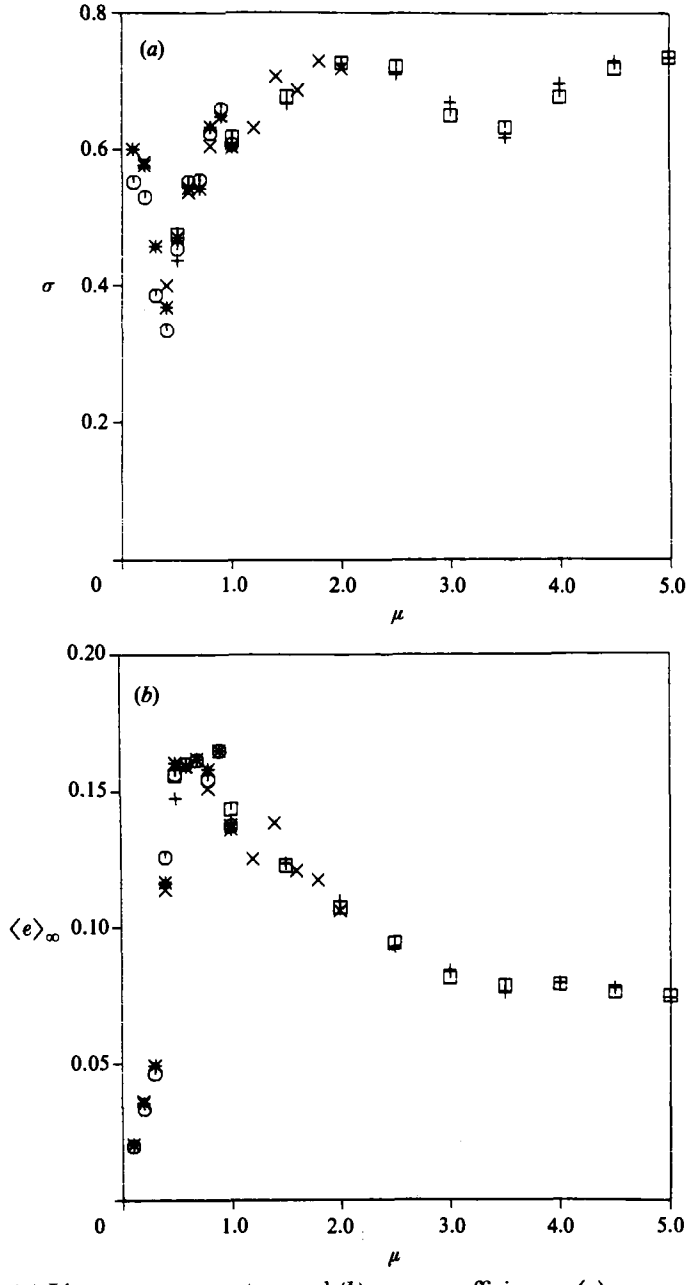

FIGURE 14. (*a*) Liapunov exponent σ, and (*b*) average efficiency, $\langle e \rangle_\infty$, versus flow strength μ for points in the chaotic region of the BV mapping calculated for 50000 cycles of the mapping, $\hat{m}_0 = (0, 1)$ and various initial conditions. (+) $x_0 = (0.9, 0)$; (*) $x_0 = (0.99, 0)$; (○) $x_0 = (0.99, 0)$. D; (×) $x_0 = (-0.99, 0)$, D; (□) $x_0 = (-0.99, 0)$. D denotes double precision.

Figure 14 shows the Liapunov exponent and average efficiency versus the flow strength calculated for 50000 cycles of the mapping for points initially in the chaotic region. The initial positions chosen in the calculations were close to one of the vortices so that prior to the transition to global chaos the particle is restricted to one of the two chaotic regions around each vortex. The behaviour of the Liapunov exponent

(figure 14*a*) is quite complex, and experiences a sharp change near the transition to global chaos ($\mu \approx 0.36$). Calculations up to a value of $\mu = 15$ show that the Liapunov exponent continues to increase slowly with increasing flow strength for $\mu > 5$. The average efficiency, in contrast, has a single maximum of $\langle e \rangle_\infty \approx 0.16$ at $\mu \approx 0.8$, indicating the existence of an optimal operating condition at which the rate of stretching per unit rate of energy dissipated is the highest on the average. (The maximum value was incorrectly reported as 0.36 in Khakhar, Chella & Ottino 1984.) The average efficiency seems to level off to a value of $\langle e \rangle_\infty \approx 0.07$ beyond $\mu = 3$ and our calculations indicate that it remains almost constant at that value up to a flow strength $\mu = 15$.

The maximum in the average efficiency is related to the T^{-1} (or μ^{-1}) decay in efficiency for large T in each half-cycle of the BV flow, which is typical of weak flows (Chella & Ottino 1985), and results from the material element aligning along streamlines. In the case of the BV flow the streamlines change at the end of the period, so that the material elements experience a relative reorientation. When μ is small, relatively little stretching takes place prior to reorientation and on the average the efficiency takes on low values; at large flow strengths the efficiency decays to low values and again the average efficiency is low. Between the limits there exists a flow strength at which the average efficiency is maximum, as was found in our calculations.

The Liapunov exponents and average efficiency calculated above provide a description of the local mixing. In the next section we study some aspects of the mixing on a global scale by considering the dispersion of particles at the lengthscale of the system.

10. Macroscopic dispersion of tracer particles

We use flow-visualization experiments to qualitatively assess the ability of the flow to disperse initially concentrated aggregates of tracer particles. We also calculate approximately the 'intensity of segregation', a statistical measure of the mixed state often used in the study of mixing (Danckwerts 1952), for the numerical experiments described above.

The dramatic contrast in mixing in the regular region to that in the chaotic region is shown in figure 15. A circular blob made up of a large number of points, and located at a fixed position in the flow (figure 15*a*), is convected by the flow. At $\mu = 0.8$ the blob is outside the chaotic region, and figure 15(*b*) shows the deformed blob after 30 cycles of the flow. The mixing in this case is poor and lengths increase linearly with the number of iterations resulting in a relatively small deformation of the blob. At a higher flow strength ($\mu = 1.0$) the chaotic region is larger so that the blob is initially inside the chaotic region and efficient dispersion of particles results, as can be seen from figure 15(*c*) which shows the blob after 24 cycles of the flow. In this case the blob does not appear continuous owing to the large amount of stretching, and relatively few points (9500) used in the visualization. To see the intricate striated structure formed on mixing a very large number of points would be required. The total time of mixing is the same in both cases, time being proportional to μN where N is the number of cycles.

Evidence for the existence of cantori is presented in figure 16 in which circular blobs of particles initially in one of chaotic regions around each vortex (figures 16*a* and *c*) are prevented from mixing uniformly over the chaotic region, presumably by cantori, when the flow strength is not much larger than the bifurcation value.

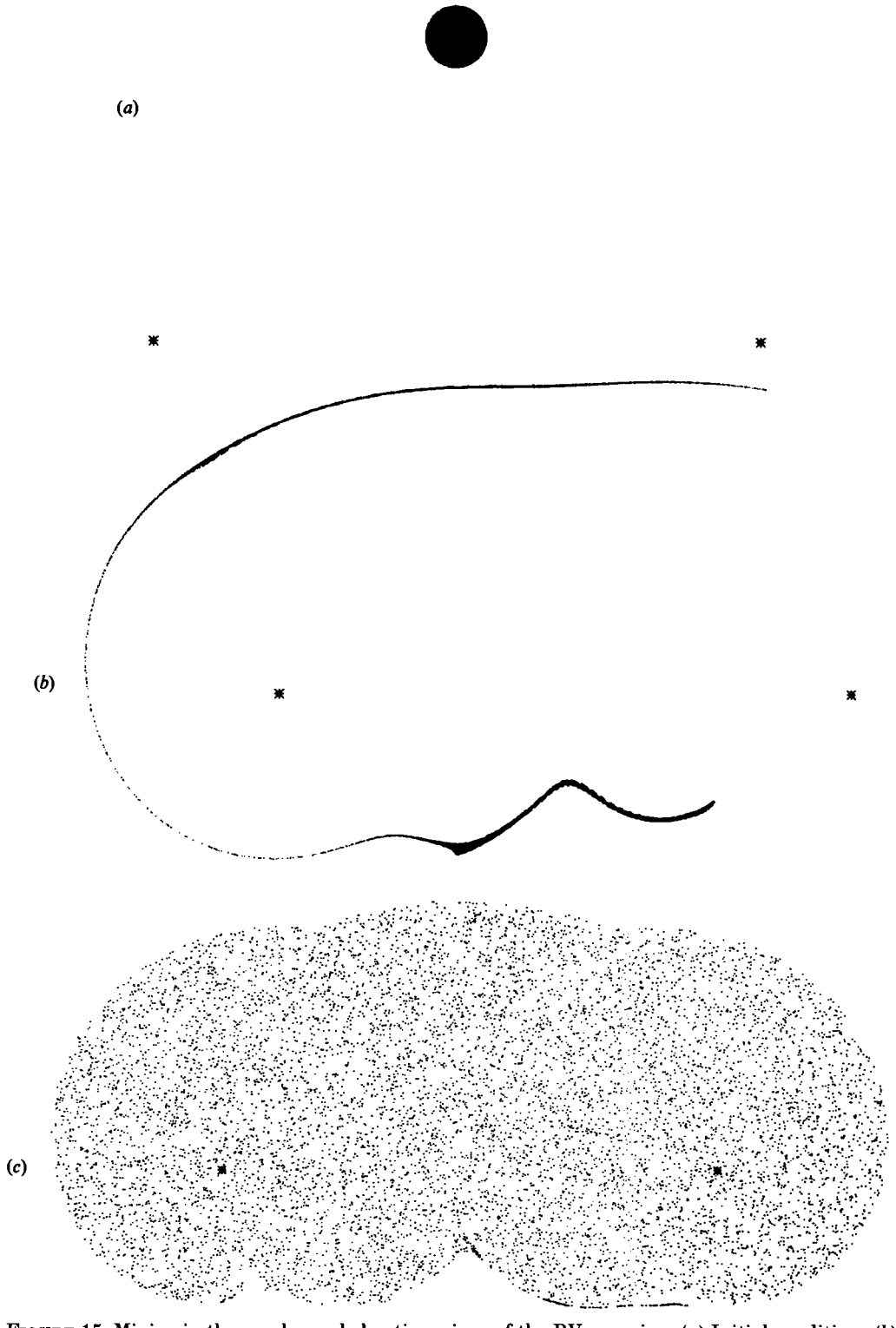

FIGURE 15. Mixing in the regular and chaotic regions of the BV mapping. (*a*) Initial condition; (*b*) and (*c*) mixed state. (*b*) Blob after 30 cycles of flow with $\mu = 0.8$, and (*c*) blob after 24 cycles of flow with $\mu = 1.0$. Note that total time of mixing μN is the same in both cases.

FIGURE 16(*a*, *b*). For caption see facing page.

FIGURE 16. Obstruction to mixing by cantori of the BV mapping for a flow of strength $\mu = 0.5$. (*b*), (*d*) show the blobs, initially as in (*a*), (*c*), after 25 cycles of the flow. Notice the non-uniform mixing over the chaotic region.

Figure 16(*b*, *d*), which shows the blobs after 25 cycles of flow, support our earlier claim that there exist two cantori which separate the figure-of-eight region from the chaotic regions around each vortex. In both cases we see that the dispersion of the particles in the chaotic region in which the blob was initially located is good; relatively few particles travel into the figure-of-eight region being obstructed by a cantorus, and almost none of the particles travel from the chaotic region around one vortex into the chaotic region around the other having to pass through two cantori. Thus the presence of cantori may prevent uniform mixing even ater the transition to global chaos. At large enough flow strengths, however, the cantori do not significantly hinder mixing as is evident from figure 15(*c*).

The state of mixedness in the above numerical experiments may be quantified in some sense by the 'intensity of segregation' (Danckwerts 1952) defined as

$$I = \frac{\langle (C - \langle C \rangle)^2 \rangle^{\frac{1}{2}}}{\langle C \rangle},$$

where C is the local concentration and $\langle . \rangle$ indicates a volume average. (The intensity of segregation is usually defined as a ratio between the standard deviation of the concentration at a given state to that at an initial state.) In the case of an actual dye experiment, the blob would remain connected for all time forming a striated structure, so that the intensity of segregation may be considered to be some measure of the distribution of striation thickness. We calculate the intensity of segregation approximately by imposing a grid of squares of side δ on the chaotic region, and defining the concentration to be the number of particles per square. For a given flow strength, grid size δ, initial size and location of the blob we obtain the intensity of segregation for increasing numbers of cycles of flow. Our calculations indicate that in most cases a rapid decrease in intensity of segregation with time takes place; it is possible, however, for the particles to be aggregated by the flow (demixed) at short times. Graphs of the intensity of segregation versus the total time (μN) for a particular set of initial conditions and different values of μ are shown in figure 17. For $\mu = 0.5$ there is initially a rapid decrease in the intensity of segregation followed by a much slower decrease to its asymptotic value. Recall that in this case cantori pose leaky barriers to transport (figure 16) so that in the first stage particles are quickly dispersed only in the chaotic region around one of the vortices bounded by a cantorus, resulting initially in a rapid decrease in the intensity of segregation. In the second stage, transport through the cantori controls the rate of mixing, and the intensity of segregation decreases slowly as more particles leak through the cantori. At higher flow strengths, the cantori do not obstruct the mixing significantly, and there is a rapid decrease in the intensity of segregation to an asymptotic value, the decrease being most rapid for $\mu = 1.0$.

The above analysis provides a description of the mixing in the Aref-blinking-vortex system, and thus some qualitative insights into similar chaotic mixing systems which are bounded, periodic and composed of weak flows. Some examples of such flows are a periodically operated journal-bearing flow (Aref & Balachandar 1985), a periodically operated cavity flow (Chien *et al.* 1986), and the flow in a Kenics® static mixer (Khakhar 1986). Though the structure of the periodic points and their bifurcations would depend on the details of the flow, the existence of positive Liapunov exponents, and a maximum average efficiency are expected to be common to all such systems.

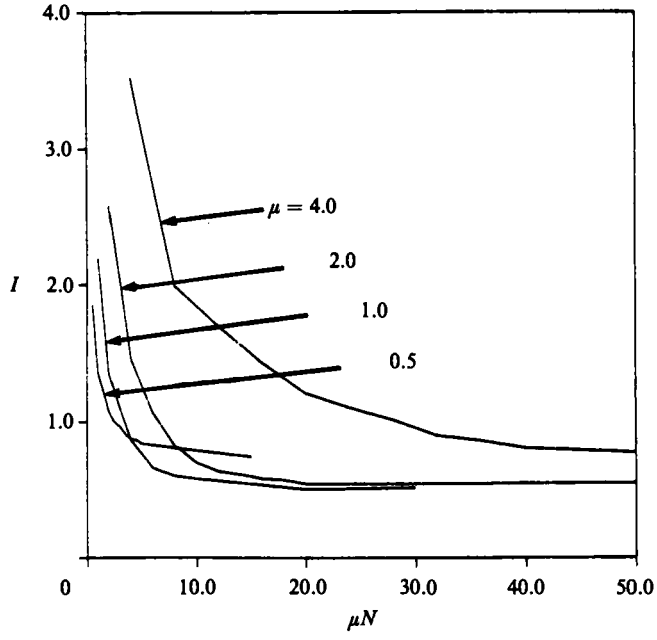

FIGURE 17. Intensity of segregation I versus total time of mixing μN for different flow strengths μ calculated for a square blob of side 0.01 initially centred at (0.99, 0). Grid size $\delta = 0.12$.

11. Conclusions

We have presented an analysis of two kinematically defined flows governed by external parameters – the extensional and the rotational strengths in the TW mapping, and the blinking time for the BV mapping. The study was motivated by our need to understand and anticipate the occurrence of chaos – and hence good mixing – in fluid flows. Even though there are many other simulations and analyses that might enhance our understanding of the operation of such systems, it is safe to say that not all aspects of the analyses, such as those usually carried out in the context of dynamical systems, will be of importance from a fluid mixing view point. Of the many unsolved mathematical questions, the size of the unmixed islands seems to be the most important; of the quantities computed in this paper, the length stretch (Liapunov exponent) and the average efficiency are the most useful from a practical viewpoint: the length stretch and area stretch in three-dimensional flows can be related to the intermaterial area which is useful for the study of mechanical mixing (Ottino & Chella 1983) and reactive mixing (Ottino 1982).

One of the main differences between two- and three-dimensional periodic flows that are chaotic is that because of the additional degree of freedom in the latter case, if KAM surfaces exist they do not act as barriers to transport owing to the phenomenon of 'Arnold diffusion' (Lieberman & Tennyson 1982). The transport in this case, however, is exponentially slow (Arnold 1983). In addition, in the case of three-dimensional flows, there is a possibility of obtaining higher flow efficiencies on the average, the maximum possible efficiency for this case being

$$e_{\max} = \sqrt{(2/3)},$$

compared to $\sqrt{(1/2)}$ for two-dimensional flows. In the case of three-dimensional velocity fields that are themselves chaotic, such as turbulent flows, the situation is more complex. Though not much can be said about the structure of the motion in such flows, it is well known that lengths increase exponentially and the motion of particles is chaotic. In fact, considering that most velocity fields of practical interest for mixing applications are three-dimensional and unsteady, and the relative abundance of chaotic systems as compared to regular systems, we expect most mixing flows to be chaotic, and much remains to be done to understand mixing in such flows. For example, future studies might focus on the dynamics of flows specified by an internal parameter, perhaps the Reynolds number, in which changes in the parameter result in changes in the flow kinematics and thus the mixing.

The authors take pleasure in acknowledging the financial support of the National Science Foundation in the form of the PYI award (CPE-8351096) and the Department of Energy (DE-FG02–ER13333). The help of D. Oliver of the Digital Image Analysis Laboratory, University of Massachusetts, Amherst, in obtaining the colour photographs is also greatly appreciated.

REFERENCES

AREF, H. 1984 Stirring by chaotic advection. *J. Fluid Mech.* **143**, 1–21.

AREF, H. & BALACHANDAR, S. 1985 Chaotic advection in a Stokes flow. *38th Annual Meeting of APS/Division of Fluid Dynamics, Tucson, Arizona, USA.* (Abstract, *Bull. Amer. Phys. Soc.* **30**, 1703.)

AREF, H. & TRYGGVASON, G. 1984 Vortex dynamics of passive and active interfaces. *Physica* **12D**, 59–70.

ARNOLD, V. I. 1983 *Geometrical Methods in the Theory of Ordinary Differential Equations.* Springer.

BENNETIN, G., GALGANI, L., GIORGILLI, A. & STRELCYN, J.-M. 1980*a* Lyapunov characteristic exponents for smooth dynamical systems and for Hamiltonian systems; a method for computing all of them. Part 1: theory. *Meccanica* March, 11–20.

BENNETIN, G., GALGANI, L., GIORGILLI, A. & STRELCYN, J.-M. 1980*b* Lyapunov characteristic exponents for smooth dynamical systems and for Hamiltonian systems; a method for computing all of them. Part 2: numerical application. *Meccanica* March, 21–30.

BERRY, M. V., BALZACS, N. L., TABOR, M. & VOROS, A. 1979 Quantum maps. *Ann. Phys.* **122**, 26–63.

CHELLA, R. & OTTINO, J. M. 1985 Stretching in some classes of fluid motions and asymptotic flow efficiencies as a measure of flow classification. *Arch. Rat. Mech. Anal.* **90**, 15–42.

CHIEN, W.-L., RISING, H. & OTTINO, J. M. 1986 Laminar mixing and chaotic mixing in several cavity flows. *J. Fluid Mech.* (in press).

DANCKWERTS, P. V. 1952 The definition and measurement of some characteristics of mixtures. *Appl. Sci. Res.* **A3**, 279–296.

GREENE, J. 1979 A method for determining a stochastic transition. *J. Math. Phys.* **20**, 1183–1201.

GUCKENHEIMER, J. & HOLMES, P. 1983 *Non-linear Oscillations, Dynamical Systems, and Bifurcation of Vector Fields.* Springer.

HELLEMAN, R. H. G. 1980 Self-generated chaotic behavior in non-linear mechanics. In *Fundamentals Problems in Statistical Mechanics*, vol. 5 (ed. E. G. D. Cohen). North-Holland.

HÉNON, M. 1966 Sur la topologie des lignes de courant dans un cas particulier. *C. R. Acad. Sci. Paris* **A 262**, 312–314.

KHAKHAR, D. V. 1986 Fluid mechanics of laminar mixing: dispersion and chaotic flows. Ph.D. thesis, University of Massachusetts, Amherst, MA 01003, USA.

KHAKHAR, D. V., CHELLA, R. & OTTINO, J. M. 1984 Stretching, chaotic motion and elongated droplets in time dependent flows. In *Advances in Rheology*, vol. 2, *Fluids* (ed. B. Mena, A. Garcia-Rejon & C. Rangel-Naifel), pp. 81–88.

LICHTENBERG, A. J. & LIEBERMAN, M. A. 1982 *Regular and Stochastic Motion*. Springer.

LIEBERMAN, M. A. & TENNYSON, J. L. 1982 Chaotic motion along resonance layers in near-integrable Hamiltonian systems with three or more degrees of freedom. In *Non-equilibrium Problems in Statistical Mechanics*, vol. 2 (ed. W. Horton, L. Reichl & V. Szebehely). Wiley.

MACKAY, R. S., MEISS, J. D. & PERCIVAL, J. C. 1984 Transport in Hamiltonian systems. *Physica* **13D**, 55–81.

OTTINO, J. M. 1982 Description of mixing with diffusion and reaction in terms of the concept of material surfaces. *J. Fluid Mech.* **114**, 83–104.

OTTINO, J. M. & CHELLA, R. 1983 Laminar mixing of polymeric liquids: brief review and recent theoretical developments. *Polymer Engng Sci.* **23**, 357–379.

OSLEDEC, V. I. 1968 A multiplicative ergodic theorem. Ljapunov characteristic numbers for dynamical systems. *Trans. Moscow Math. Soc.* **18**, 187–231.

RISING, H. 1986 Mixing and chaos in model flows. Ph.D. in progress. Department of Mathematics, University of Massachusetts, Amherst, MA 01003, USA.

TRUESDELL, C. & TOUPIN, R. A. 1960 The classical field theories, vol. III/1. In *Handbuch der Physik* (ed. S. Flügge). Springer.